ABSTRACT

PRODUCTION AND CHARACTERIZATION OF COMPOSITE NANO/MICRO SIZED PARTICLES BY RAPID EXPANSION OF SUPERCRITICAL SOLUTIONS (RESS) CO-PRECIPITATION

by

Beidi He

Nanoscale composites of hexahydro-1, 3, 5-trinitro-1, 3, 5-triazine (RDX) and polymer binders were produced by co-precipitation using rapid expansion of supercritical solutions (RESS). The binders used in this study are poly (vinylidene fluoride-*co*-hexafluoropropylene) (VDF-HFP_{22}), polystyrene (PS) and 7-amino-4-methyl coumarin (AMC). The RDX/VDF-HFP_{22} and RDX/PS co-precipitated nanoparticles were characterized by Field Emission Scanning Electron Microscopy (FE-SEM) and Transmission Electron Microscopy (TEM). The average size of produced nanoparticles is *ca.* 100 nm. TEM analysis of RDX/PS nano-composite shows a core-shell structure with RDX as the core material and the shell consisting of the polymeric binder. X-ray Powder Diffraction (XRPD) analysis indicates polycristalline structure of RDX in the product with a crystallite size of 42 nm. The content of RDX in the composite particles is in the range 70-73% by mass as determined by Gas Chromatography-Mass Spectroscopy (GC-MS) and by XRPD.

Micronized composites of ibuprofen and bio-compatible polymer binders were produced by co-precipitation in rapid expansion of binary supercritical solutions (RESS). The binders used in this study are poly-L-lactic acid (PLLA), poly (lactic-co-glycolic acid) (PLGA), and polyethylene glycol (PEG). The recrystallized particles of pure

ibuprofen as well as produced by ibuprofen co-precipitation with a polymer binder were characterized by optical microscopy. The average ibuprofen particle sizes are 1-3 microns depending on the process conditions. The particle size increases proportionally to the cubic root of the solute concentration in the supercritical solution in CO_2. The co-precipitated ibuprofen/polymer particle size is in the range of 3-10 microns. *In vitro* dissolution rates were measured at ambient temperature as well as at 37 ℃. Polymer coated ibuprofen particles produced by RESS co-precipitation dissolve in water at ambient temperature from 10 to 20 times faster than the original ibuprofen powder. At 37 ℃ the dissolution is from 2 to 3 times faster compare to the original powder. The acceleration of the dissolution rate is due to the much smaller particle size as well as the presence of polymer layers which prevent particle agglomeration.

PRODUCTION AND CHARACTERIZATION OF COMPOSITE NANO/MICRO SIZED PARTICLES BY RAPID EXPANSION OF SUPERCRITICAL SOLUTIONS (RESS) CO-PRECIPITATION

by
Beidi He

A Dissertation
Submitted to the Faculty of
New Jersey Institute of Technology
in Partial Fulfillment of the Requirements for the Degree of
Doctor of Philosophy in Materials Science and Engineering

Interdisciplinary Program in Materials Science and Engineering

August 2015

.

APPROVAL PAGE

PRODUCTION AND CHARACTERIZATION OF COMPOSITE NANO/MICRO SIZED PARTICLES BY RAPID EXPANSION OF SUPERCRITICAL SOLUTIONS (RESS) CO-PRECIPITATION

Beidi He

Dr. Lev N. Krasnoperov, Dissertation Advisor — Date
Professor of Chemistry and Environmental Science, NJIT

Dr. Victor Stepnov, Dissertation co-Advisor — Date
Senior Scientist, U.S. Army, ARDEC, Picatinny, NJ

Dr. Rajesh N. Dave, Committee Member — Date
Distinguished Professor of Chemical Engineering, NJIT

Dr. Haim Grebel, Committee Member — Date
Professor of Electrical and Computer Engineering, NJIT

Dr. Zafar Iqbal, Committee Member — Date
Research Professor of Chemistry and Environmental Science, NJIT

BIOGRAPHICAL SKETCH

Author: Beidi He

Degree: Doctor of Philosophy

Date: August 2015

Undergraduate and Graduate Education:

- Doctor of Philosophy in Materials Science and Engineering,
  New Jersey Institute of Technology, Newark, NJ, 2015

- Bachelor of Science in Materials Science and Engineering,
  Tianjin University, Tianjin, People's Republic of China, 2008

Major: Materials Science and Engineering

Presentations and Publications:

B. He, and L. N. Krasnoperov, "Production of composite micronized ibuprofen by rapid expansion of supercritical solutions (RESS) co-precipitation," *Drug Development and Industrial Pharmacy* (submitted).

B. He, V. Stepanov, H. Qiu, and L. N. Krasnoperov, "Production and characterization of composite nano-RDX by RESS co-precipitation," *Propellants, Explosives, Pyrotechnics*, DOI: 10.1002/prep.201400249.

To my husband, Jianfeng, who gives me love, support, and encouragement.
To my daughter, Sophie, who gives me hope and courage.

ACKNOWLEDGMENT

I wish to express my deepest gratitude to Dr. Lev Krasnoperov, for his invaluable guidance, and precious advice as my doctoral dissertation advisor. His knowledge and mode of thinking guided me through my doctoral research. I also wish to give my thanks to Dr. Victor Stepanov for his countless technical support and valuable discussions as my doctoral dissertation co-advisor.

I am greatly thankful to Dr. Rajesh Dave, Dr. Haim Grebel and Dr. Zafar Iqbal for their efforts and valuable comments as members of the committee. It is my honor to have them as my committee members. I am very grateful to Dr. Hongwei Qiu for evaluating my samples by TEM imaging. My special thanks go to Mr. Yogesh Gandhi for his help and warm friendship.

At last, I am very thankful to the teaching assistantship from NJIT, which financially supported me for completing my graduate study.

TABLE OF CONTENTS

TABLE OF CONTENTS
(Continued)

Chapter **Page**

LIST OF TABLES

LIST OF FIGURES

LIST OF FIGURES
(Continued)

Figure **Page**

LIST OF FIGURES
(Continued)

CHAPTER 1

INTRODUCTION

1.1 Supercritical Fluid Technology for Particulate Matter Engineering

Supercritical fluids have been widely studied for the last three decades on their applications in materials preparation and processing. One of the most distinguishable properties of supercritical fluids is the tremendous change in the solvation power upon variations of temperature and pressure. The solvation power is closely related to the density of a supercritical solution which significantly varies with pressure at a given temperature. By tuning the external temperature and pressure the solvation power changes dramatically, which makes supercritical fluid an ideal solvent for materials dissolution and precipitation.

Supercritical fluid (SCF) technology has been widely used in particle engineering due to processing versatility unavailable with conventional solvent-based techniques. A wide range of chemical compounds can be chosen as supercritical solvents. Among them, carbon dioxide (CO_2) has become the most widely used. Carbon dioxide is inexpensive, nontoxic, and has relatively mild critical conditions, making it especially suitable as a processing medium.

Numerous SCF-based approaches have emerged for the formation of ultrafine particles. These technologies can be divided into two principal motifs. Some use SCFs as a solvent while the others use SCFs as an anti-solvent. Rapid expansion of supercritical solutions (RESS) technology is one of the most widely used processes

utilizing SCFs as the solvent, which has been employed for the production of ultra-fine nano-sized and micron-sized powders (1-7). The approach utilizes strong dependence of the solvent strength of the SCFs on both temperature and pressure. As a result, by variation the process parameters the size and the morphology of the precipitated material produced by RESS could be modified. The pre-expansion pressure and temperature control the solubility of the solute in the supercritical carbon dioxide, which control the particle size. The expansion nozzle geometry as well as temperature and pressure in the expansion vessel control the size as well as the morphology of the produced particles. Expansion of supercritical solutions leads to drastic pressure and temperature drops, resulting in the supersaturation levels above 10^7 (8). At such high supersaturations, formation of small particles is favored, as the critical nucleus size can be as small as a single molecule (9). In addition, since the pressure change travels at the speed of sound (10) right after the nozzle where most particles are formed, the uniform conditions might result in a relatively narrow particle size distribution.

The RESS method in producing small particles is limited by the material's solubility in supercritical fluid. For processing materials that are poorly soluble in SCFs, a commonly used alternative is to use a SCF as an anti-solvent. Their effectiveness as an anti-solvent stems from their high diffusivity in liquids, whereby precipitation can be rapidly achieved by the expansion of the liquid solution with an SCF (11). Supercritical anti-solvent precipitation (SAS) technology is a common form of processing utilizing this phenomenon (12).

1.2 Supercritical Fluid Technique for Particle Coating

Particle coating has attracted significant interest because by combining different materials having different physical and chemical properties to form composites, new functionality or improved properties of the known materials could be achieved. However, conventional wet coating method introduces organic solvents which are toxic and difficult to remove. In the case of dry coating (13), one requirement is that the core material and the coating material need to be pre-manufactured to form small particles. This imposes a strict limit on the particle size. Also, it stems from the application of dry coating process to form thin layer of coating film, and the process is complicated.

Coatings of nano-sized powders encounters several complications. Traditional methods such as water-based slurry coating become much less effective with very small particles. One issue is the difficulty in the dispersion of nanoparticles as they commonly exhibit a strong tendency to form agglomerates. This can result in a very non-uniform distribution of binder in the coated material. Another complication stems from the poor stability of nanoparticles in liquid suspensions. Ostwald ripening, which becomes significant at such small particle sizes, can detrimentally alter the particle size distribution. In a study aimed at characterizing the microstructure of slurry coated nanocrystalline RDX, it was shown that during coating of this material with a wax binder, which was achieved by a traditional slurry coating process, the RDX underwent extensive ripening (14).

Therefore, supercritical fluid technology is also applied in the field of small

particles coating. There are several types of techniques for particle coating using the supercritical fluid processing: Supercritical anti-solvent (SAS), Particles from gas saturated solutions (PGSS), and Rapid expansion of supercritical fluid (RESS).

In SAS (15), the coating material is dissolved in a conventional organic solvent, in which the core particles are suspended. Then a high-pressure supercritical fluid is injected into the solution, which causes the solution to expand. In this process, the core material needs to be pre-manufactured and an organic solvent is involved. In PGSS (16), a supercritical fluid is saturated with a liquid coating material. The core particles are also suspended in the liquid coating material. Particles are formed by rapid expansion of the saturated solution through a nozzle. This process is operated at moderate pressures as compared to RESS. It needs the supercritical fluid to be highly soluble in the liquid phase, which makes amorphous polymers suitable to be the coating material. Again, the core material is also pre-manufactured.

In RESS, the coating material would be extracted by a supercritical fluid to form a supercritical solution. Then the solution rapid expands through a nozzle. Deposition of thin, uniform coatings by expansion of supercritical solutions has been previously reported. Tsutsumi *et al.* (17) successfully used the RESS technology to coat paraffin wax onto submicron catalyst particles with a thickness of the paraffin layer of *ca.* 40 nm. Mishima *et al.* (18) employed the RESS process to effectively encapsulate *ca.* 15 μm protein particles in polymers. Glebov *et al.* (19) used RESS to produce polymeric films on fused silica plates and metal (Al, Mg) powders. A key distinction of the approach investigated in this work is that the core material is formed

during the same processing step as the coating, while in the reported studies the core materials was pre-manufactured.

Manufacturing of a composite material by dissolution of both components in supercritical fluid to make a binary solution had also been reported. In several studies (18, 20), a semi-batch process was used, where CO_2 first was saturated with the ingredients (the drug and the coating material) in confined vessels. After that, the mixture of the solution was expanded through a nozzle. In this approach, the amount of the material produced in one cycle is limited by the saturators' volumes as well as the solutes solubility in supercritical carbon dioxide. Moreover, in this approach, the conditions are changing during the expansion process which complicates the assessment of the impact of the process conditions on the product properties.

In the approach used in this study, we developed a continuous extraction and expansion system which overcomes the restrictions associated with the limited volume as well as the limited solubility of the solutes in supercritical carbon dioxide.

1.3 Particles Coating in Pharmaceutical Applications

Bioavailability is an important factor in drug design and medical applications of a drug (21). Many successfully designed and synthesized prospective chemical substances either have limited functionality as drugs or are even completely useless because of their low bioavailability (22-24). One of the factors that limit bioavailability of some drugs is low solubility in water (25-27). For poorly water-soluble drugs, their rate of absorption in the gastrointestinal tract depends on

the dissolution rate. Therefore, enhancement of the dissolution rate might improve the efficiency of certain drugs in the biological environment. One of the ways to increase the dissolution rate is the reduction of the particle size. Micronization is one of the commonly used methods to improve the drug dissolution rate. Traditional methods for micronization include grinding, milling, and spray-drying. However, these approaches result in wide particle size distribution and often introduce undesirable organic solvent residue (28). Even much smaller particles, if manufactured, are to be protected from agglomeration. This involves usage of a bio-compatible excipient with good solubility in water. Such a formulation, consisting of a very small drug particles (micron and submicron range) mixed with a bio-compatible polymer matrix is expected to dissolve much faster than larger (10–100 μm) particles of a low solubility substance.

However, production of such compositions using standard techniques encounter difficulties associated with the problems of homogeneous mixing of micronized powders (29-31). In this work we suggest a technology which allows preparation of homogeneously micronized mixtures in a single technological step. In addition, the proposed technology is free from organic solvents, which is beneficial both from the point of view of strict regulations on the residual organic solvents (32) as well as environmental contamination issues.

Ibuprofen is a widely used pain relieving drug. However, this substance has poor solubility in water which has a negative impact on the drug performance. Low solubility delays the pharmaceutical action. To achieve faster response, the

formulations use larger amounts of the active pharmaceutical ingredients (5). The increase of the dissolution rate might mitigate the problem. Ibuprofen has a relatively high solubility in supercritical carbon dioxide (33). In this study we applied the technique to the production of micronized ibuprofen/biocompatible polymer composites.

Among prospective substances to be used as supercritical fluid solvent, carbon dioxide has several advantages. Carbon dioxide is non-toxic, economic; the production can be arranged in an environmentally friendly closed loop process. Previous studies on exploration of RESS technology for drug micronization (34-37) had been reported. One of the major problem encountered is agglomeration of the produced particles (5). Attempts to sieve micronized ibuprofen produced by RESS through a 250 μm mesh or physically mixing it with lactose did not improve the rate of dissolution. A thin polymer coating of the micron-sized particles could protect the drug particles from agglomeration in the composition. In addition, utilization of a highly soluble polymer might facilitate separation of the particles in the process of dissolution. Such polymer coated micron and submicron particles could be produced by a modification of the RESS technology. Rapid expansion of binary supercritical solutions of a drug with a highly soluble biocompatible polymer could be a solution of the agglomeration problem.

1.4 Objectives of Research

In a preceding study, the RESS technology was employed to produce high quality and

purity nanocrystals of hexahydro-1, 3, 5-trinitro-1, 3, 5-triazine (RDX), a common military high explosive used in numerous munitions. The nanocrystalline form of RDX showed a dramatic decrease in the initiation sensitivity to mechanical stimuli including shock and impact, which are key sources of accidental initiation (38). High explosives are rarely used in their pure form, rather, coating with a polymeric or wax binder is typically required. In this work, an alternative method for encapsulating RDX nanocrystals with a binder was investigated. The aim was to augment the existing RESS process with in-situ coating of the newly formed RDX nanocrystals with a polymeric binder. To accomplish this, the earlier RESS method (1) was modified by dissolving a polymeric binder together with RDX in supercritical CO_2. This would necessarily cause both solutes to co-precipitate during RESS. In order to verify whether the desired structure was obtained with core RDX nanocrystals coated with a thin polymeric layer, transmission electron microscopy was employed.

In this work, the RESS technology was also employed to produce high quality and purity microcrystals of ibuprofen as well as ibuprofen and biopolymer composites using continuous rapid expansion of binary supercritical solutions. With the fundamental understanding of the structures and morphology obtained by the co-precipitation of RDX and polymer binders. The continuous RESS technique to the pharmaceutical application is scaled-up. Ibuprofen was known to have 1000 times higher solubility as compared to RDX in supercritical carbon dioxide. The experiments are designed to apply the continuous RESS method for ibuprofen and some bioavailable polymers co-precipitation. The dissolution kinetics of the produced

materials was studied to evaluate the pharmaceutical benefits. Comparison of the dissolution behavior of the co-precipitated material with the unprocessed ibuprofen provided additional information on the morphology of the materials produced by the co-precipitation process.

CHAPTER 2

CO-PRECIPITATION OF RDX AND POLYMERS COMPOSITE BY RESS

2.1 Materials

Pure RDX was obtained by recrystallization of commercial RDX from acetone to eliminate impurities (mainly 12% of HMX in the initial material). VDF-HFP_{22}, a poly(vinylidene fluoride-co-hexafluoropropylene) copolymer with 22 mol % hexafluoropropylene, was purchased from 3M, with a purity of 99+%, and a MW of 85,000 g/mol. Polystyrene was obtained by dissolution of Styrofoam #6 in toluene with subsequent precipitation (MW of *ca.* 250,000 g/mol, purity 99%). AMC (7-amino-4-methyl-coumarin) (99.9%) was purchased from AnaSpec Inc., with a purity of 99.9%. Common organic solvents were used as purchased. Acetone (99.5+%, ASC grade) was purchased from Sigma Aldrich. Toluene (99.9%, HPLC grade) was purchased from Fisher Scientific. Carbon dioxide (99.8+%, bone dry grade) was purchased from Scott Specialty Gases. Liquid CO_2 was supplied in cylinders with a siphon tube and pressurized with helium to 103 bar.

2.2 Experimental Set-up

The experimental setup is schematically shown in Figure 2.1. It consists of a carbon dioxide supply system, a Thar P-50 dual piston pump (Thar Designs Inc.) with a maximum discharge pressure of 350 bar and a maximum flow rate of 50 g/min, an RDX extraction vessel (1.27 cm ID, 35 cm long), a binder extraction vessel (1.27 cm ID, 35 cm long), and an expansion system.

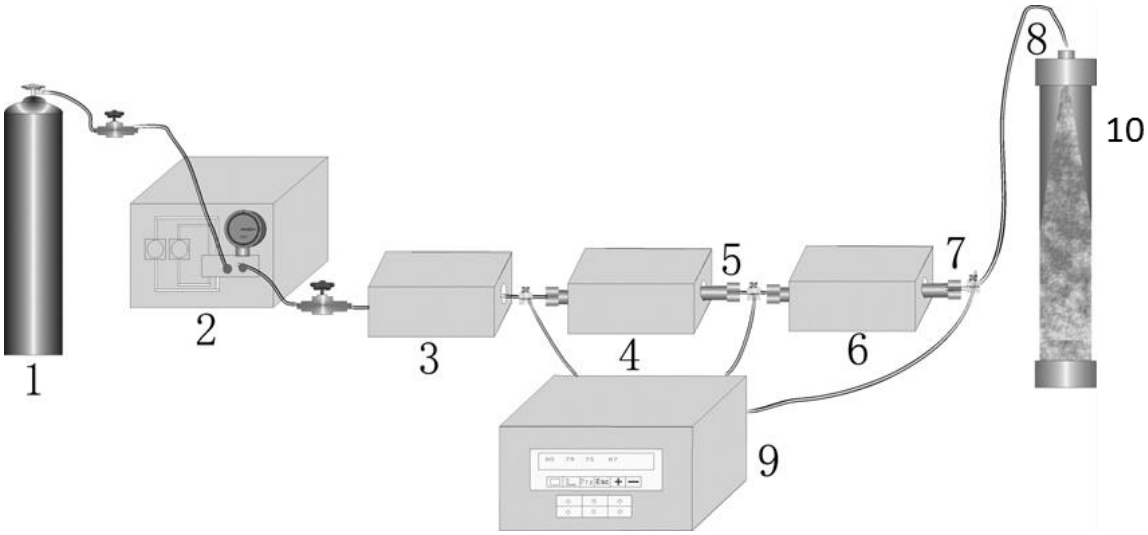

Figure 2.1 The experimental set-up. 1: CO_2 cylinder (liquid CO_2, pressurized with helium, equipped with educator tube); 2: Dual piston pump; 3,4,6: Ovens; 5: RDX extraction vessel; 7: Binder extraction vessel; 8: Nozzle; 9: Temperature monitor; 10: Expansion chamber.

All connections are made of 3.175 mm OD stainless steel tubing and SS Swagelok unions. The two extraction vessels are heated by two temperature controlled ovens. The connecting tubings are heated by variac powered heating elements. Four K-type 3.175 mm thermocouples are used to measure temperatures of the system elements. The thermocouples were placed in the RDX extraction vessel, inside the connecting tubing between the two extraction vessels using a union tee fitting (Swagelok), inside the tubing after the second extraction vessel again using a union tee fitting, and inside the supply tubing 50 mm before the stainless steel expansion nozzle. The cylindrical expansion/collection vessel prevented the co-precipitated RDX/binder powders from being influenced by moisture from entrainment of ambient air. The expansion vessel is made of transparent acrylic resin

with a 40 mm ID and is 36 cm long. The nozzle has an orifice with the inner diameter of 100 μm and a length of 3 mm.

Liquid carbon dioxide withdrawn through the dip tube on the supply cylinder was fed to the pump. The pump output pressure was chosen by adjusting the mass flow rate using the pump controller. The pump piston heads and the incoming carbon dioxide were chilled to -5 ℃ for maximum pumping efficiency. Downstream from the pump the liquid carbon dioxide was preheated to the desired temperature in an oven prior to being fed to the extraction vessels. The RDX and polymer extraction vessels were packed with 3 mm diameter glass beads on which the respective solutes were deposited. The beads were used to significantly increase the surface area to accelerate dissolution of polymers in supercritical CO_2. In the first vessel, the glass beads were coated with solid RDX (by wetting with a solution of RDX in acetone with subsequent drying). In the second vessel, the beads were coated with a polymer binder (either VDF-HFP_{22} deposited from a solution in acetone or polystyrene deposited from a solution in toluene). Supercritical solution of RDX and the binder is transferred through a heated, 3.17 mm stainless steel tube to the nozzle assembly where it is expanded to ambient pressure. The nozzle was uniformly heated with embedded heating elements to prevent blockage due to accumulation of dry ice as a result of drastic cooling of the feed solution during expansion. The product is collected on wax paper or glass substrates placed at the bottom of the expansion vessel.

2.3 Procedure

To preload the binder onto the glass beads in the vessel, 1 ml of binder solution (0.2 g VDF-HFP_{22} dissolved in 10 ml of acetone or 0.2 g polystyrene dissolved in 10 ml of toluene) was added drop-wise to the binder extraction vessel and dried in ambient air flow (vacuum pumped). RDX solutions were prepared by dissolving 0.4 g RDX in 10 ml of acetone. The coating of the beads was performed in a similar manner, 2 ml of the RDX solution was added drop-wise to the RDX extraction vessel also filled with glass beads, followed by drying with ambient air flow for 2 min. After drying, the heaters were turned on to reach the desired temperatures. The RDX vessel temperature was varied in the range 70-80 ℃. The binder vessel temperature was varied in the range 100-110 ℃. The expansion nozzle was maintained at 50 ℃. After temperature stabilization for *ca.* 10 min, the high-pressure dual piston pump was turned on and liquid CO_2 was pumped at a constant flow rate. To collect adequate quantities of the products, typical runs lasted 15 min.

The initial material collected on the bottom of the expansion vessel was solid carbon dioxide (powdered dry ice) with entrained nanoparticles of RDX/binder. The product was left for *ca.* 1 h for carbon dioxide to sublime. The residual powder on wax paper or glass substrates was weighed and stored for further characterization. The RDX and binder vessels were disconnected from the system and weighed before and after each run to monitor the rate of consumption of RDX and the binder. The experimental conditions used in the preparations of the samples are summarized in Table 2.1.

Table 2.1 Summary of Co-precipitated Nano-particles Produced by RESS

No.	Component	Temperature / ℃ (mean)	Pressure /bar (mean)	wt. % RDX
I	RDX	52	200	100
II	RDX/VDF-HFP_{22}	48	200	70
III	RDX/PS	53	205	72
IV	RDX/PS	50	150	72
V	RDX/PS	51	130	72

2.4 Physical Properties of Co-precipitated RDX/polymer Composite

2.4.1 X-ray Powder Diffraction Analysis

X-ray Powder Diffraction (XRPD) analysis of prepared materials was performed using a Philips PW3040 X-Ray Diffractometer. Cu Kα radiation was employed for crystal structure analysis as well as crystallite size analysis in the RDX/VDF-HFP_{22} nano-composites. Furthermore, quantitative analysis of constituents in the product materials was performed with XRPD.

For quantitative determination, samples of the precursor RDX from 1.2 to 90 mg were scanned for calibration. The scattered intensity was recorded in the range $26° \leq 2\theta \leq 30°$ in steps of 0.008 ° with a counting time of 0.96 s per step. The RDX powder was dissolved in acetone (1.5 g RDX/20 g acetone). For calibration, one to

thirty drops of the RDX solution were placed on quartz plates; the weights of the produced polycrystalline RDX were measured after acetone evaporation. A 15 mm beam width, a 1/2 ° incident beam divergence slit, and a 1/2 ° diffracted beam antiscatter slit were used. The X-ray diffractograms of different mass of the RDX (Figure 2.2) precursor showed orthorhombic structure.

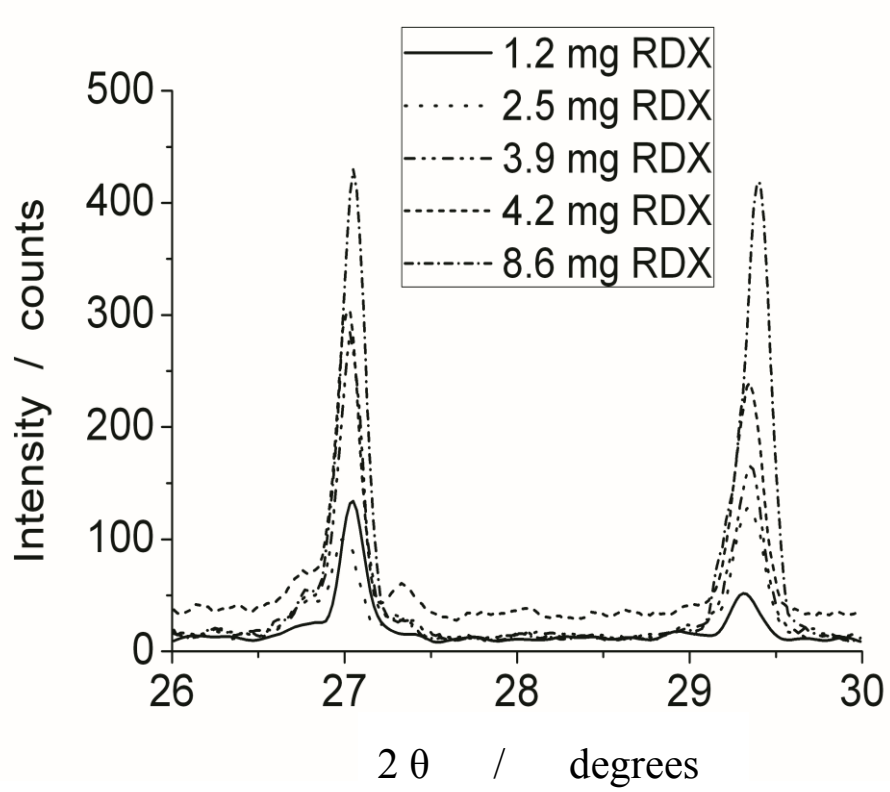

Figure 2.2 XRPD pattern of precursor RDX.

The major characteristic diffraction peaks of RDX are at 2 θ = 12.95, 25.21, 26.77 and 32.17 °, which are in conformity with the crystal faces of (111), (131), (113) and (223) of RDX (39). After Fourier transform smoothing and the background subtraction, the diffraction peaks were integrated. The peak area is increasing linearly with the mass of RDX (Figure 2.3).

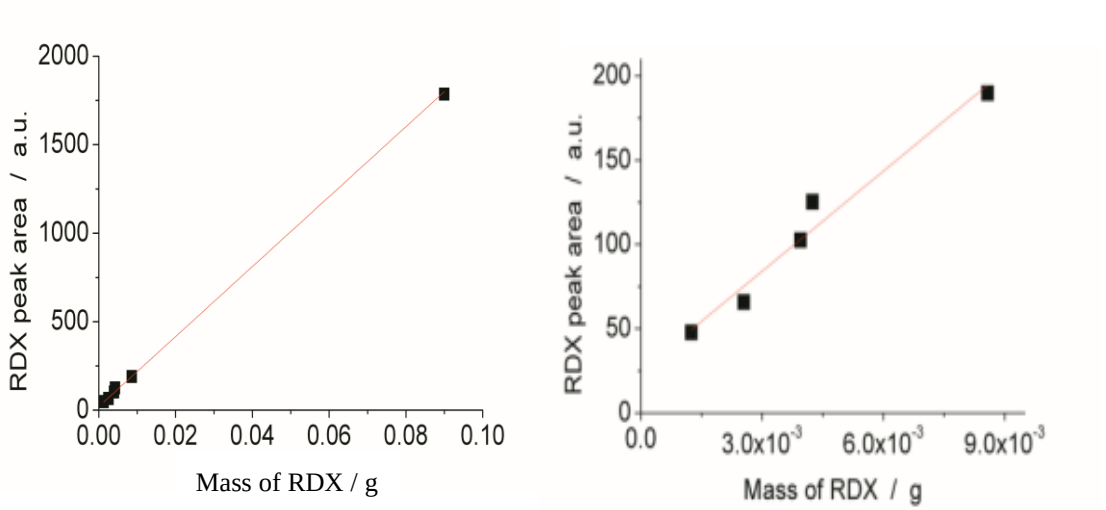

Figure 2.3 Calibration curve of the integrated RDX peak areas from XRPD measurements. RDX mass is in the range of 1.2-90 mg.

The precursor RDX, the RESS recrystallized RDX (sample I), VDF-HFP_{22} polymer, and the RESS co-precipitated RDX/VDF-HFP_{22} composite (sample II) were scanned by XRPD in series for crystal structure study. Specimens of each material (0.15 g) were scanned separately in a 4 cm long × 2 cm wide × 0.5 cm deep stainless steel sample holder. Data was recorded in the range $10° \leq 2\theta \leq 45°$, which is the full pattern range for standard RDX in the database (39) as shown in figure 2.4. The samples were scanned in steps of 0.019 ° with a counting time of 1s per step. A 15 mm beam width, a 1 ° incident beam divergence slit, and a 1 ° diffracted beam antiscatter slit were used. Figure 2.5 shows an expansion in the diffraction angle range of 26-30 °. The XRD diffractogram of the VDF-HFP_{22} film shows amorphous broad halo which represented its average polymer chain separation at 2θ = 12-22 °. In Figure 2.4d, every single peak was broadened due to the small RDX crystallite size in the composite.

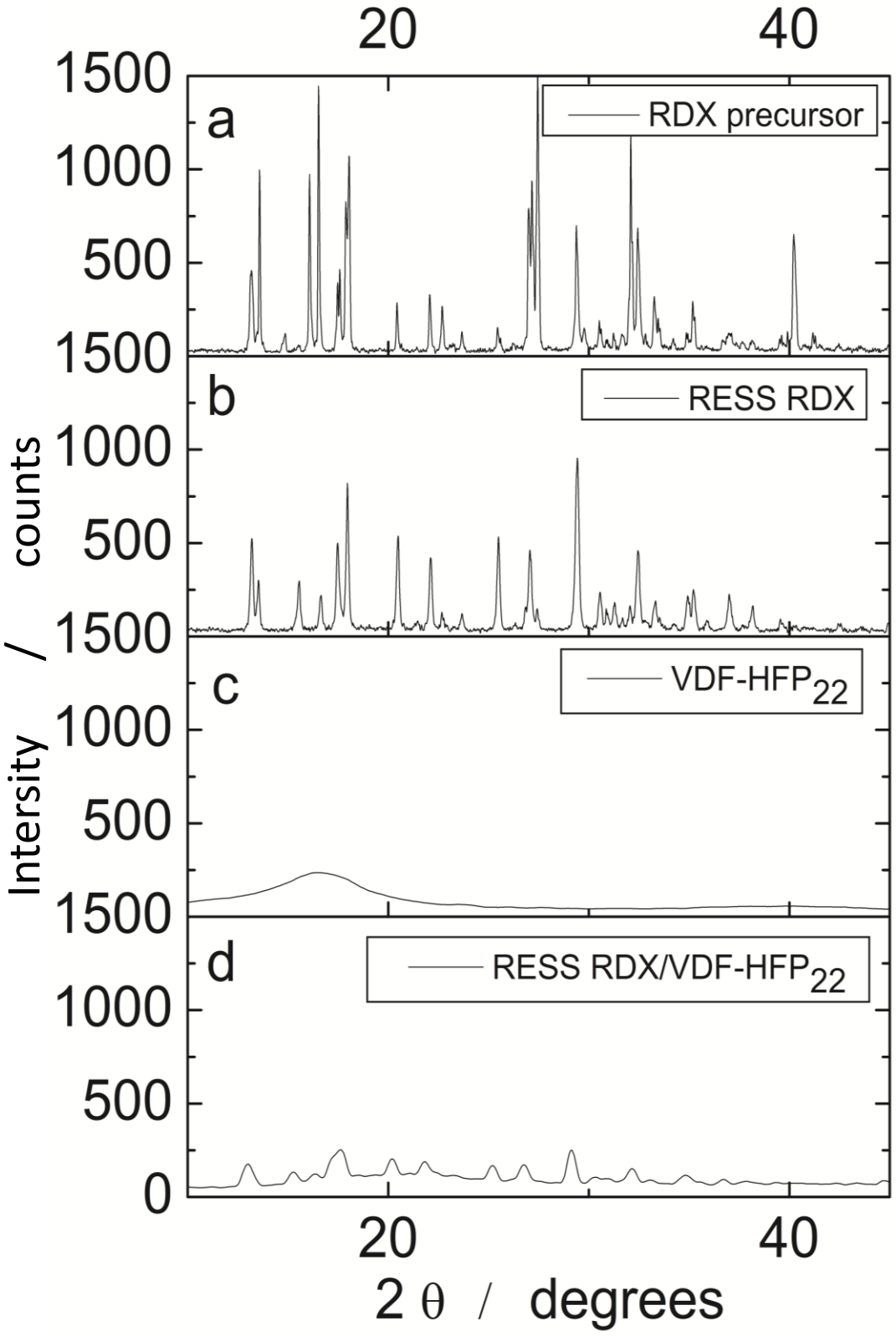

Figure 2.4 XRPD patterns of 0.15 g RDX precursor, RESS recrystallized RDX (sample I), VDF-HFP_{22} and RESS co-precipitated RDX/VDF-HFP_{22} (sample II).

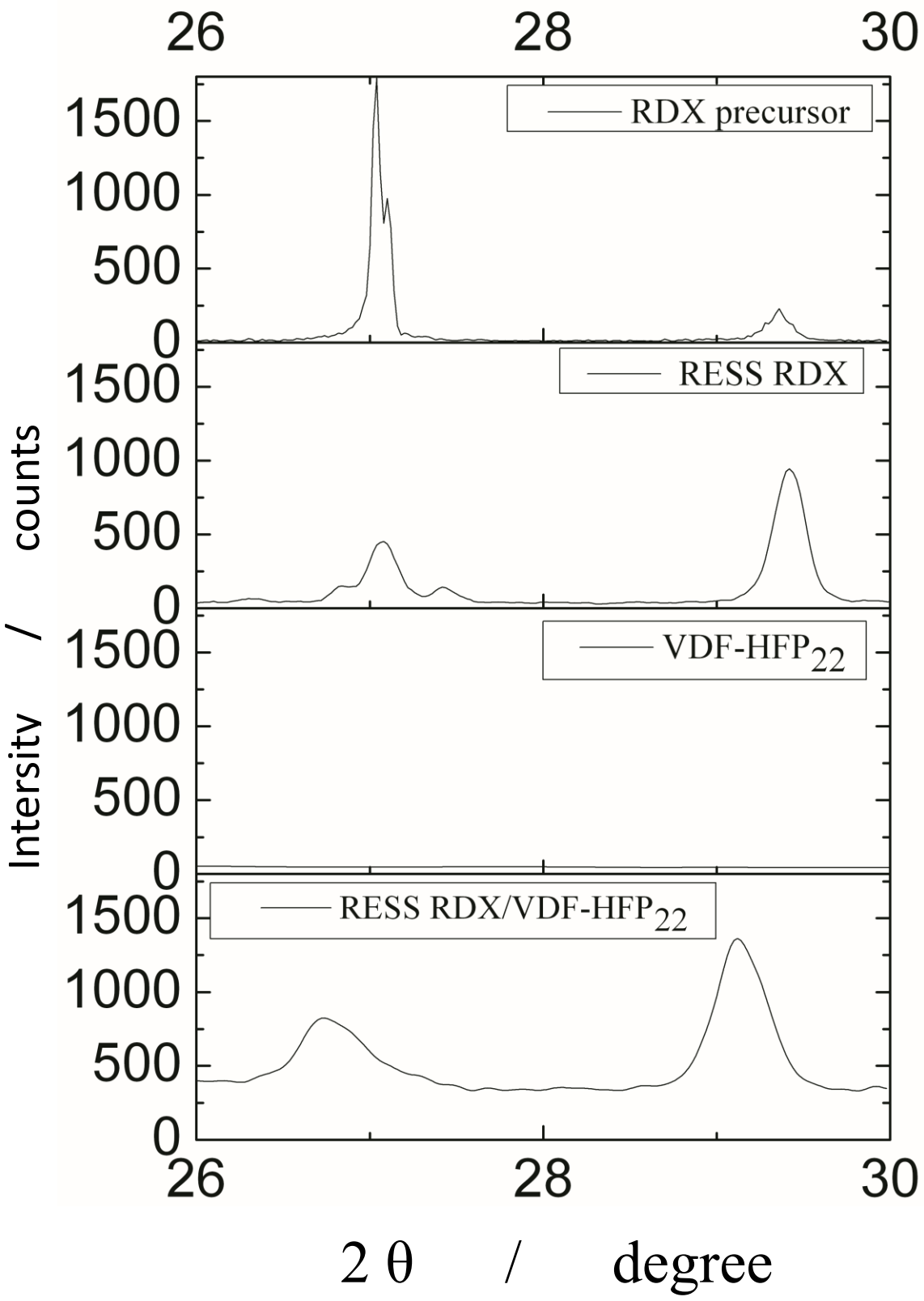

Figure 2.5 XRPD patterns in smaller angle range of 0.15 g RDX precursor, RESS recrystallized RDX (sample I), VDF-HFP_{22} and RESS co-precipitated RDX/VDF-HFP_{22} (sample II).

Figure 2.5 also showed amorphous broad halo as a background which represented the average chain separation of coated VDF-HFP_{22}. Compared to the precursor (large) RDX crystals, the diffraction line in the nano-RDX is broadened and has lower peak intensity. By integrating the peak area of RDX/VDF-HFP_{22} in the diffraction angle range of 26-30 °, the RDX mass content in the nano-composite was determined as about 73 wt.%.

According to the Scherrer equation (40), the diffraction lines are broadened due to the small size of the crystallites. The crystallite dimensions can be calculated using equation 2.1:

$$Dv = \frac{K\,\lambda}{\beta s\,cos\theta} \tag{2.1}$$

where D_v is the volume weighted crystallite size. The parameter K is the Scherrer constant, which is usually considered to be equal to 1; λ is the wavelength of the X-rays used; β_s is the broadening due to the small crystallite size; θ is the X-ray diffraction angle. The broadening due to the microstrain in the crystals, β_{str}, as well as the broadening due to the instrument, β_{inst}, (which is usually set to 0.07) should also be considered (41). Assuming that the shapes of the broadened diffraction peaks for both the size and the strain components are Lorentzian, the total integral breadth (defined as the ratio of the peak area to the peak height) is obtained by adding the three contributions together:

$$\beta t = \beta s + \beta str + \beta inst \quad (2.2)$$

According to Stokes and Wilson (42), the broadening due to the microstrain can be estimated using equation 2.3:

$$\beta str = 4\,\varepsilon\,\tan(\theta) \quad (2.3)$$

Here ε is a measure of the microstrain which usually originates from the crystal defects.

Combining equations (2.1), (2.2), and (2.3), the Williamson-Hall plot (43) can be drawn:

$$\frac{(\beta t - 0.07)\cos(\theta)}{\lambda} = \frac{1}{Dv} + \frac{4\,\varepsilon \sin(\theta)}{\lambda} \quad (2.4)$$

Therefore, by plotting (β_t - 0.07) cos(θ) / λ vs. 4 sin(θ) / λ, d_v and ε can be determined.

Table 2.2 Scherrer Peak Broading Analysis Parameters (Sample II in Table 2.1, Composite RDX/VDF-HFP_{22})

2 θ /degree	**2 sin(θ)/λ** /nm^{-1}	**FWHM** /degree	**($\beta=\beta_{str}+\beta_s$)** /radians	**β cos(θ)/λ** /nm^{-1}
12.9	2.27	0.660	5.15×10^{-3}	3.29×10^{-2}
25.2	2.83	0.682	5.34×10^{-3}	3.38×10^{-2}
26.7	3.00	0.705	5.54×10^{-3}	3.50×10^{-2}
32.1	3.59	0.756	5.99×10^{-3}	3.74×10^{-2}

The full width at half maxima of the peaks (FWHM) for the four main peaks of the RDX scattering pattern at 12.95, 25.21, 26.77 and 32.17 ° (2θ) are listed in Table 2.2.

The peaks were integrated and their areas were divided by the peak heights. After that, the instrument broadening factor was subtracted. Figure 2.6 shows the Williamson-Hall plots for RDX precursor (44), RESS produced nano-RDX (44), and co-precipitated composite RDX/VDF-HFP_{22}. The volume-weighted RDX crystallite size in the composite determined from the Williamson-Hall plot is ca. 42 nm.

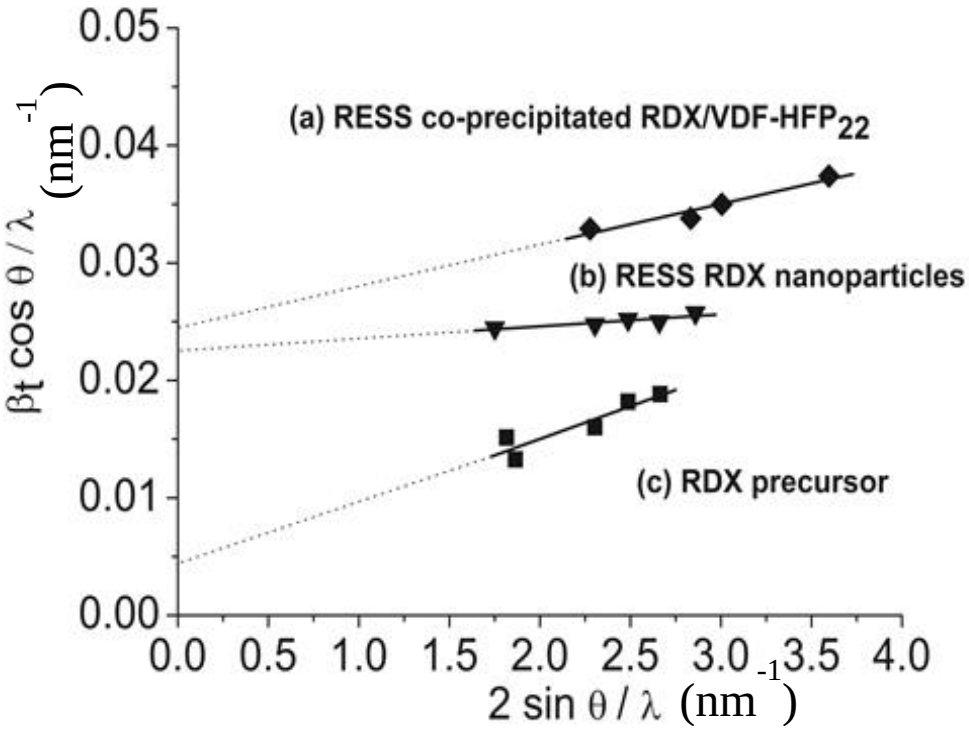

Figure 2.6 Williamson-Hall plot for (a) RESS co-precipitated RDX/VDF-HFP_{22} (material II), (b) RESS recrystallized RDX (44), and (c) unprocessed RDX (44).

This is similar to the crystallite size of pure nano-RDX (44 nm (44)), but

smaller than the particle size observed by SEM. This indicates that there are multiple RDX crystallites inside the composite particles. This observation is in accord with the previous study (at somewhat different conditions, 80 ℃ and 280 bar), where the crystallite size of the RESS recrystallized RDX was 44 nm (Figure 2.3b (44)). Both the nano-composite and nano-RDX crystallite size are much smaller than the crystallite site of unprocessed RDX (44).

The Williamson-Hall plot for the composite nano-particles also indicate larger internal strain in the crystallites compared to the nano-RDX but smaller than in the precursor (as determined from the slopes) of the Williamson-Hall plot Figure 2.6.

2.4.2 Gas Chromatography - Mass Spectroscopy Analysis

Gas Chromatography (GC) with Mass Spectroscopy (MS) analysis of prepared materials was performed using an HP 6890 series GC and an HP 5973 MS using electron impact ionization. Ultra-high grade purity Helium (99.999%, Airgas) was used as the carrier gas. A 30 m × 0.25 mm ID × 0.25 μm film thickness HP-5MS capillary column was used. The column flow was 1.0 ml/min. The column temperature was held at 150 ℃ for 30 min. The injector temperature was 150 ℃ and the detector temperature was 250 ℃. The inlet was fitted with a double tapered liner and set in splitless mode. The purge valve opened and split vent flow increased to 100 ml/min at 1.5 min after the injection to sweep any vapors remaining in the liner out to the split vent. The mass spectra were acquired over the 12-550 m/z mass range.

Standard solutions of RDX were prepared and analyzed to determine the retention time and the RDX mass-spectrum.

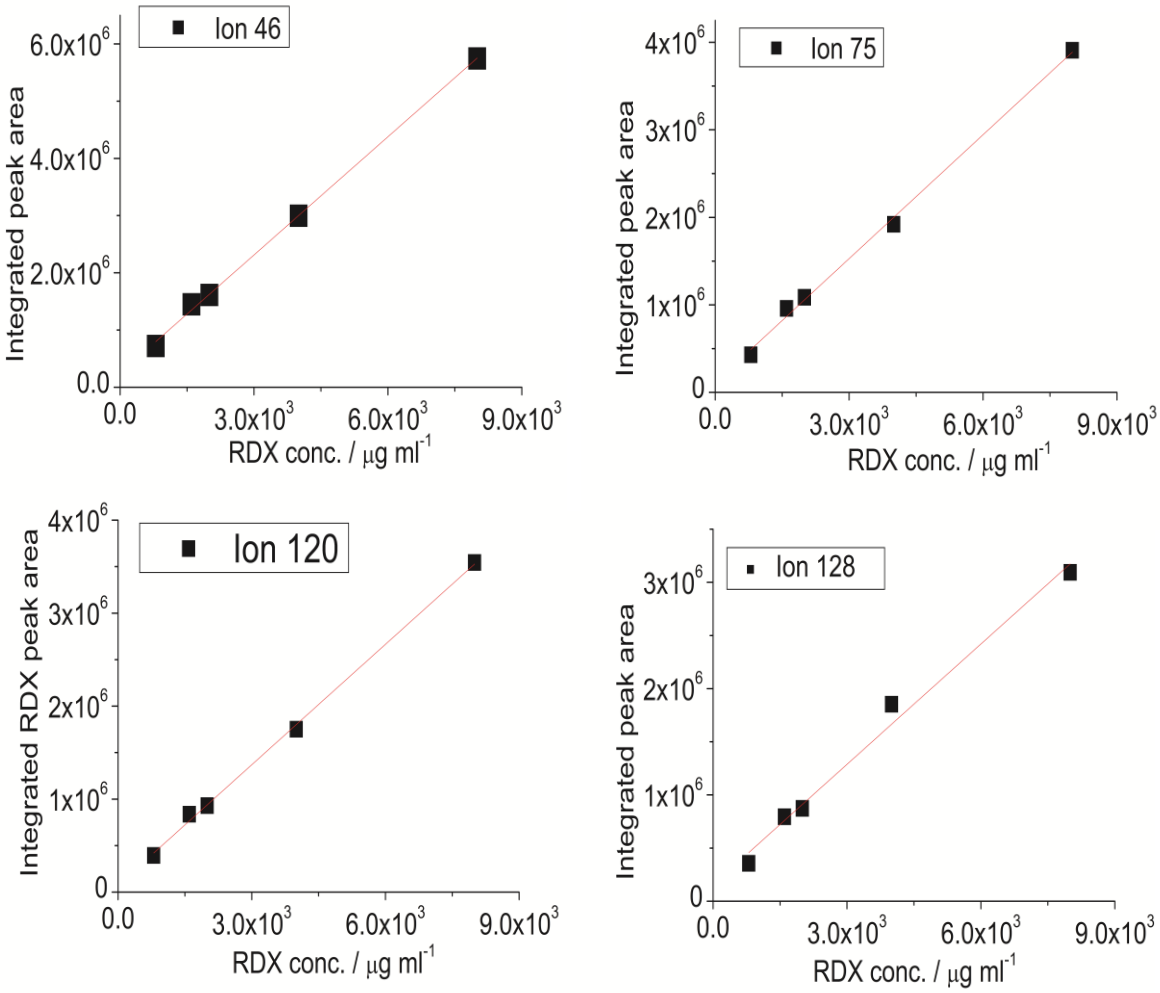

Figure 2.7 RDX five point calibration plot of m/z = 46, 75, 120, and 128 MS signals.

RDX was identified correctly using the NIST mass-spectra database search. The retention time and the quantification ions which were used subsequently for RDX determinations are 15.4 min; and m/z = 128, 120, 75, and 46. All quantifications were based on the peak area of the MS signal. The stock solutions of RDX were made by weighing 0.1 g (± 0.0001 g) of RDX and dissolving it in 5 ml of acetone in a volumetric flask. The mass spectrums were taken and the retention times were determined at different concentrations of RDX in the solutions. The calibration

standards were prepared by diluting the stock solution with acetone in 1 ml volumetric flasks. Five calibration standards were made containing RDX at concentrations between 800 and 8000 μg/ml.

Peak areas of the analytes were then used to construct the calibration curves as shown in Figure 2.7. Regression analysis was used to assess the linearity of the analytical method. Five point calibration curves were constructed which produced correlation coefficients (R^2) greater than 0.994. The RESS co-precipitated RDX/VDF-HFP_{22} and RDX/PS composites were analyzed to determine the mass content of the two components. The RDX concentrations were determined using the calibration plots. Figure 2.8 shows total ion chromatograms (TIC) in the calibration measurements.

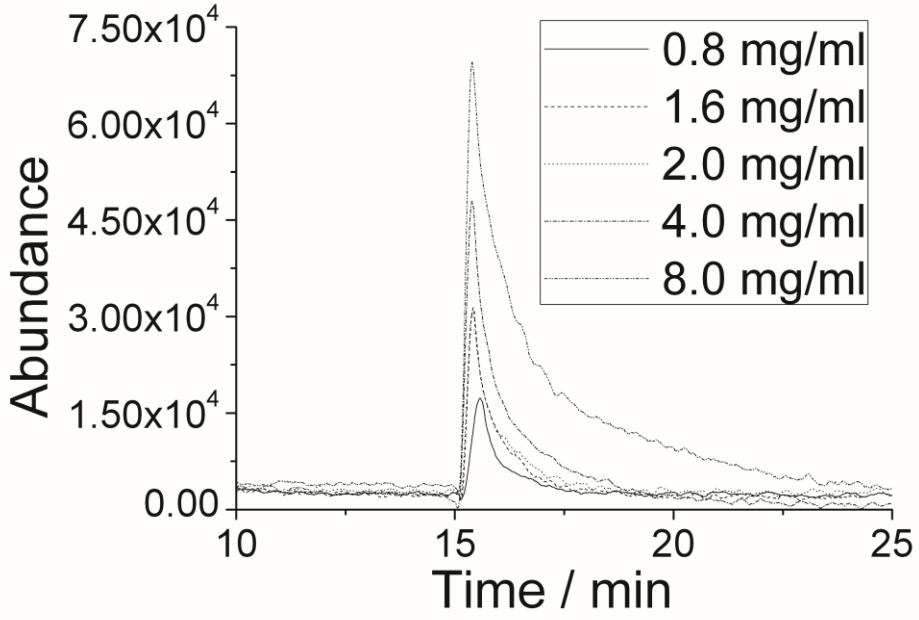

Figure 2.8 GC-MS total ion chromatograms for RDX standard solutions in the range of 0.8-8.0 mg/ml.

The RDX peak has a retention time of 15.4 min. The same method was used to

analyze sample II RDX/VDF-HFP_{22} nano-composite (Figure 2.9), which was dissolved in acetone with concentration of 80 μg/ml, 100 μg/ml, and 2000 μg/ml, respectively. GC-MS analysis requires much smaller amounts of the powders (ca. 2 mg vs. ca. 150 mg). By this analysis (based on the integration of the peak areas of ions with m/z values of 46, 75, 120, and 128), the RDX mass content in the RDX/VDF-HFP_{22} composite was determined as 70%, in good agreement with the XRD quantitative analysis, which yielded 73% RDX mass content. The RDX/PS nano-composite (sample III) and RDX/AMC nano-composite were evaluated using the same method (Figure 2.10, Figure 2.11).

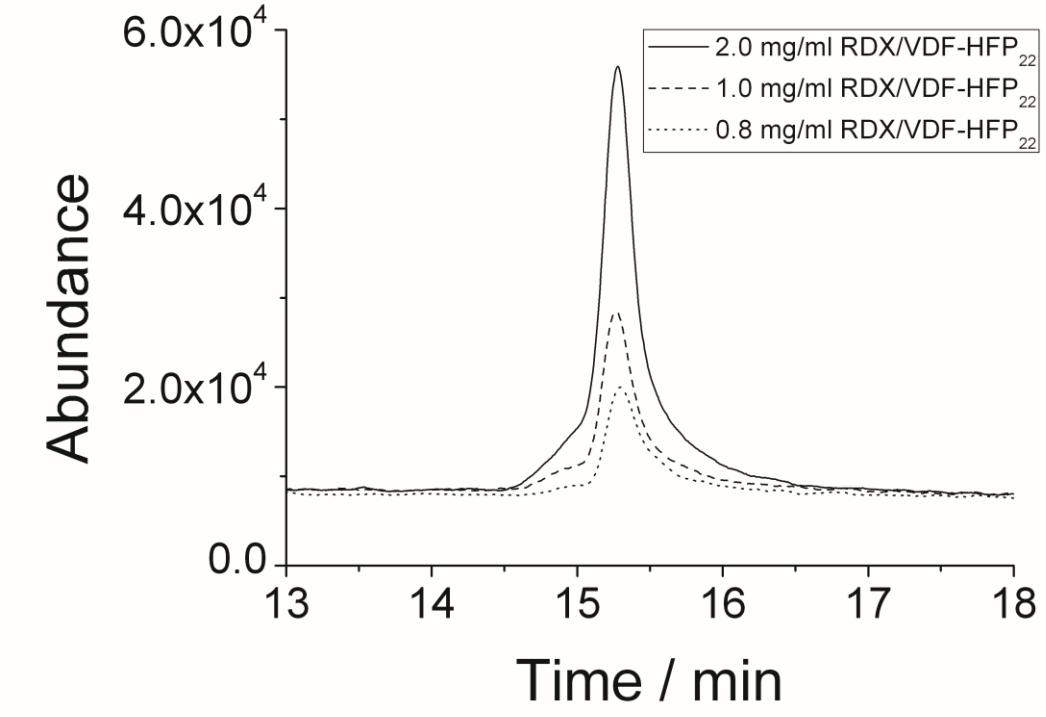

Figure 2.9 GC-MS total ion chromatograms for RESS co-precipitated RDX/VDF-HFP_{22} nano-composite sample II (200 bar, 48 ℃) dissolved in acetone with concentrations 0.8, 1.0, and 2.0 mg/ml.

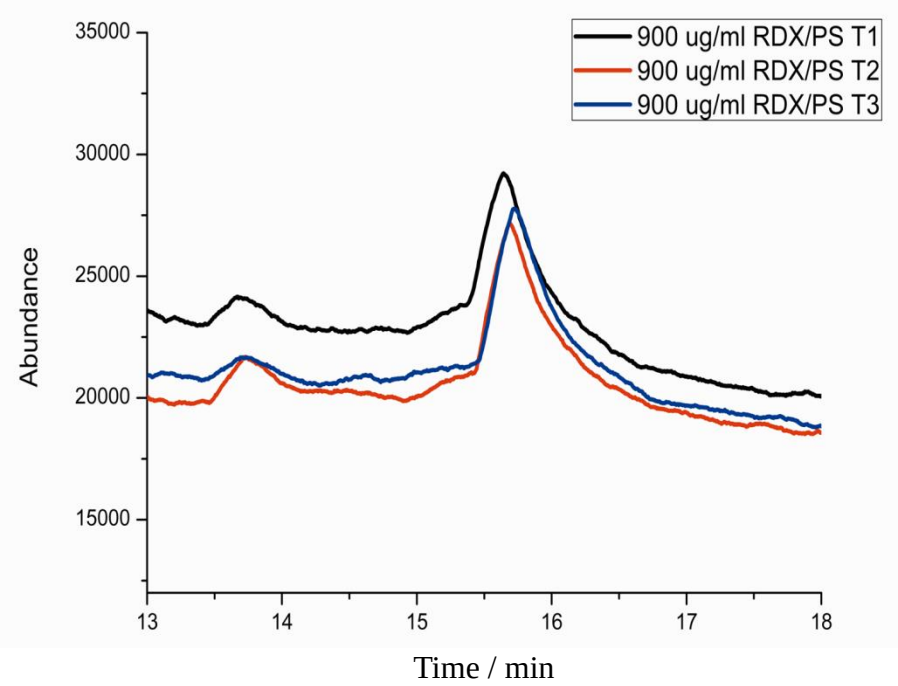

Figure 2.10 GC-MS total ion chromatograms for RESS co-precipitated RDX/PS nano-composite dissolved in acetone with concentration of 900 μg/ml.

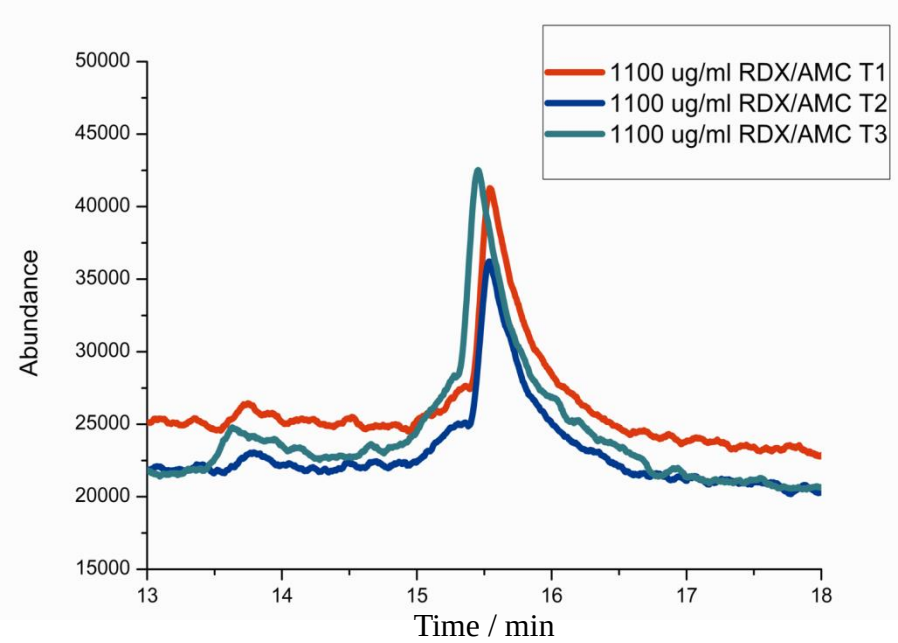

Figure 2.11 GC-MS total ion chromatograms for RESS co-precipitated RDX/AMC nano-composite dissolved in acetone with concentration of 1100 μg/ml.

By subtracting the background and integrating the peak area, the measured RDX mass content in RDX/PS and RDX/AMC nano-composite are *ca.* 72% and 80%, respectively.

2.4.3 GC-MS Analysis on RDX/AMC Nanocomposite

2.4.3.1 Preparation and Storage of Standards. Stock standard solutions of RDX (3000 μg ml^{-1}) and AMC (1000 μg ml^{-1}) were prepared in acetone. The solution was sonicated in an ultrasonic bath (20 min) until a homogeneous and clear solution was formed. The stock solution was stored at room temperature for a maximum of 1 month. Before use, standard working solutions were prepared by diluting appropriate amounts of the stock solution.

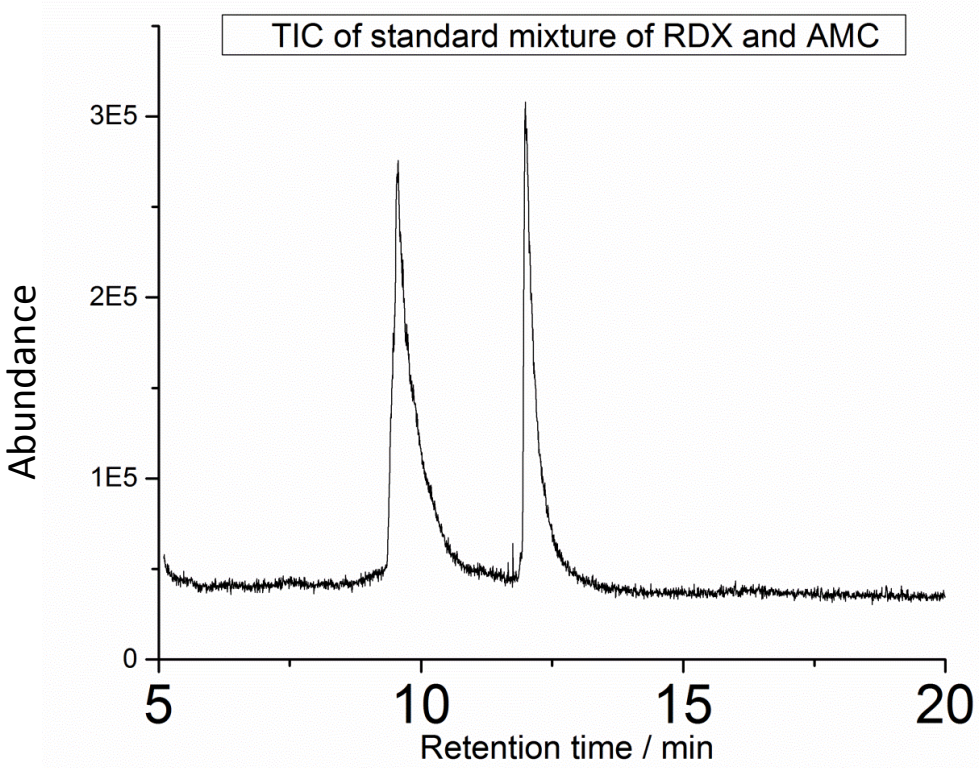

Figure 2.12 Total ion chromatogram of the RDX and AMC standards. Concentration of analytes injected: RDX 500 μg ml^{-1}; AMC 166 μg ml^{-1}.

The temperature of the GC injector was held at 150 ℃. Temperature of the MS detector was at 230 ℃. The oven temperature was set at 150 ℃, held for 5 min, increased to 170 ℃ at 5 ℃ min^{-1}, held for 2 min, then to 230 ℃ at 8 ℃ min^{-1} and held for 5 min. The peak areas were used to quantify the analytes.

The chromatogram of the standard mixtures of RDX and AMC under the adopted GC conditions using the HP-5MS is shown in Figure 2.12. Good separation of RDX and AMC was achieved. No column degradation was observed.

2.4.3.2 Linearity. The sensitivity of the GC method was tested by injecting standard mixtures of the analyte (25-3000 µg ml^{-1}). The calibration curves obtained by plotting the integrated peak area against the concentration of the respective standards were found to be linear over the range 25-3000 µg ml^{-1}. The correlations coefficients are 0.9994 for RDX and 0.9972 for AMC (Table 2.3). Good linearity was obtained for the same analytes when assessed over 6 days. The calibration plot is shown in Figure 2.13.

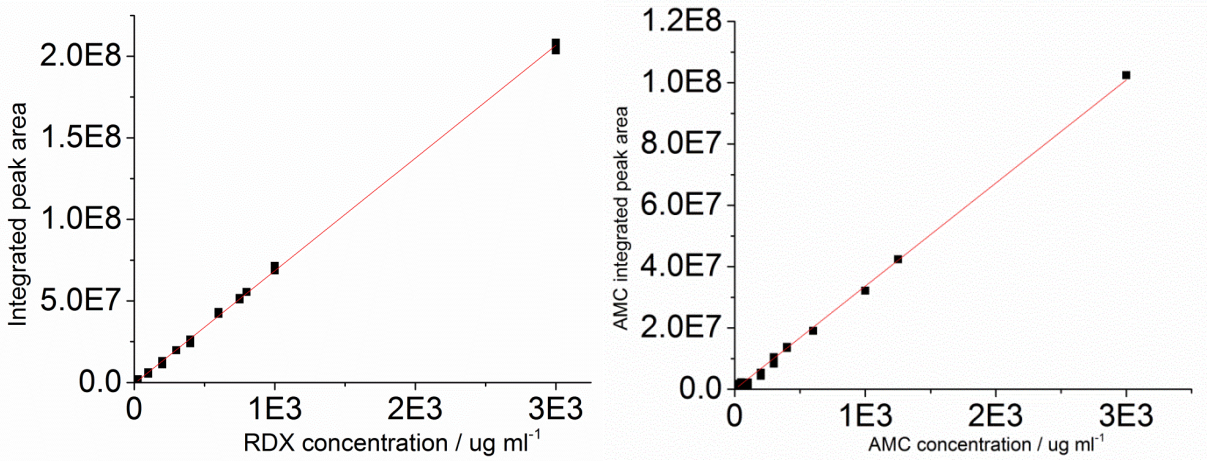

Figure 2.13 Calibration plots of the GC method used in the measurements.

2.4.3.3 Reproducibility Study. The reproducibility of the retention time was assessed by injecting the same standard solution (25, 50, 100, 200, 300, 400, 600, 800, 1000 μg ml^{-1}) over the period of 8 days. Each standard was injected 5 times, which resulted in total 45 data points. The relative standard deviation (RSD) for the retention time obtained for RDX is 0.37%, and for AMC is 0.97%. The low RSD values indicate that the retention times were highly reproducible.

Table 2.3 Calibration Data of the GC Method Used

Analyte	**Regression equation**	**Linearity**	**Correlation coefficient**
μg ml^{-1}		μg ml^{-1}	r^2
RDX	$y = 6.8 \times 10^4 x$	25-3000	0.9994
AMC	$y = 3.3 \times 10^4 x$	25-1000	0.9972

2.4.4 Evanescent Excitation Microscopy of RESS Co-precipitated RDX/AMC Powder

The experimental set-up is shown in Figure 2.14. An attempt to gain information on the morphology of the particles produced by the method using optical microscopy was made. The idea of the experiment was as follows. By precipitation of a binary solution of RDX with a fluorescent dye and by comparing usual microscopic images with the images taken in the fluorescence one might derive some conclusions on whether there are particles made of different component or not.

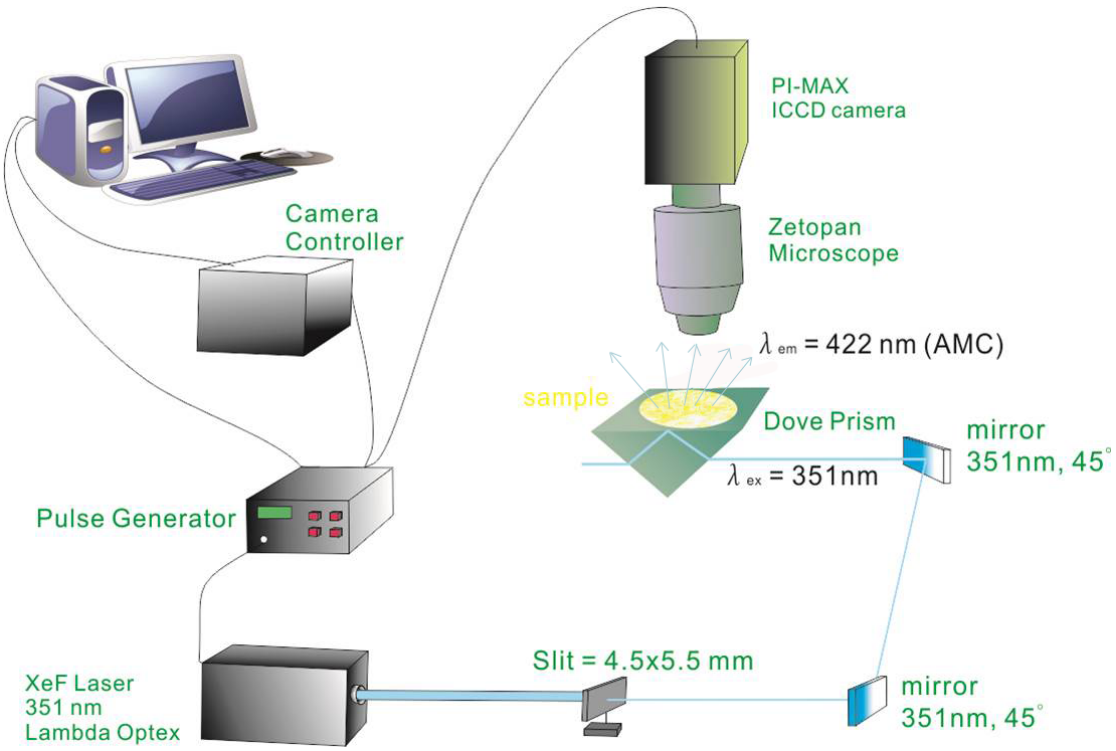

Figure 2.14 Evanescent excitation microscopy experiment set-up.

To this end, the total internal reflection fluorescence microscopy was performed for RESS co-precipitated RDX/AMC nanoparticles. AMC (7-amino-4-methyl coumarin) is a highly fluorescent material which could be excited with a 351 nm laser light. Thin layers of the sample powders were placed on the diagonal face of a right angle fused silica prism. The laser beam is entering the prism through a smaller face, is being refracted, completely internally reflected from the diagonal face, and lives though the second smaller face, as shown in Figure 2.14. Outside the diagonal face of the prism exponentially decaying electromagnetic wave is formed (evanescent wave). The effective thickness of the evanescent field is about the wavelength. This approach allows avoiding the illumination of the objective lens with the laser pulse, and provides sensitive detection of the fluorescence of the AMC

dye molecules. The fluorescence occurs at 422 nm (blue light). The image is recorded using the gated ICCD camera.

Amino methyl coumarine (AMC) has short fluorescence lifetime of 1.9 ns (45). The gate width of the ICCD camera was 2 μs, the laser pulse was triggered within the gate. The images were taken in fluorescence using laser excitation as well as common images in light scattering using traditional light sources.

2.4.4.1 Sample Preparation. Nano-RDX/AMC samples made at 214 bar, 51.5 ℃ and 198 bar, 37.3 ℃ were examined. 0.1 mg of either powder was placed on the prism, 5 μl of acetone was used to spread the powder to make a flat surface to make a sample.

Images of blank prism were acquired on daily bases to make a blank comparison. All of the blank images had "zero" (less than 5 counts/pixel after 1000 laser pulses) intensity in the photon counting mode.

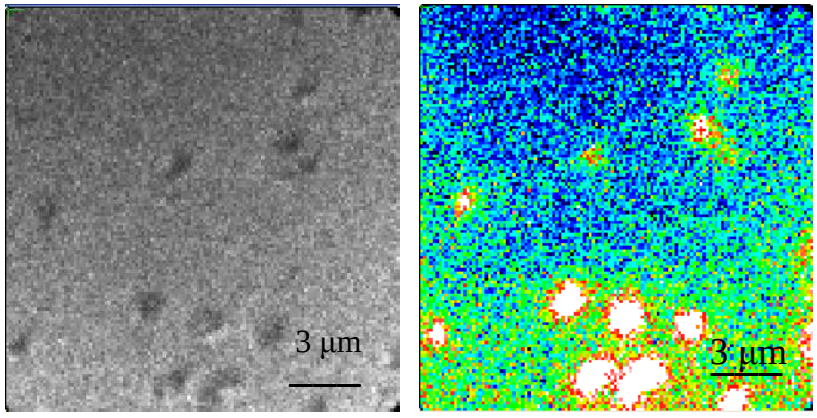

Figure 2.15 RESS co-precipitated nano RDX/AMC. Left – traditional microscopy; right – evanescent excitation, the images are taken in fluorescence. Photon counting maximum intensity: 205 counts/binned pixel. Gate width 2 μsec. gain 255, discrimination thresholds 175-700, 8×8 binning pixel, microscope magnification 56×10 = 560.

Bulk RDX was also evaluated. It did not show any detectable fluorescence. In the photon counting mode, the maximum intensity of fluorescence was ca. 500 counts/pixel. It should be noted, that the size of the particles shown in in Figure 2.15 is not resolved, the particles are broadened by diffreaction and not perfect focussing. Therefore, the amount of matter could not be evaluated from these images.

Three locations of each sample were examined. Comparing the optical microscopy images and the fluorescent microscopy images, all particles in the field of view are fluorescent as shown in Figure 3.0, which means all the particles contain AMC, no pure RDX was found. Although a number of images have been acquired, no more definitive conclusions about the particle morphology (such as the component partitioning and spatial distribution) have been derived.

2.4.5 Scanning Electron Microscopy Analysis

Microscopy of produced materials was performed using a LEO 1530VP Field Emission Scanning Electron Microscope (FE-SEM). Nanoparticles were deposited on a 1 cm × 1 cm glass slide, which was mounted on a 1.3 cm diameter aluminum stub using an adhesive carbon tape and were sputter coated with carbon to a thickness of *ca.* 200 Å using a Bal-Tec MED 020 HR Sputter Coater. The generated images are shown in Figure 2.16. Figure 2.16a shows the morphology and the size of the RESS recrystallized RDX nanoparticles. Figure 2.16b is the SEM micrograph of the sample II, produced with both RDX and VDF-HFP_{22} loaded in the vessels. As it can be seen, the RDX nanoparticles have a relatively narrow size distribution. The distribution functions were obtained by manually measuring each particle area using Image-Pro

Plus 6.0 software and calculating their equivalent diameter. For nano-RDX, the frequency was plotted vs. the particle diameter from 0 to 400 nm and the increment of 50 nm. Total of 291 particles from three SEM images of the same sample were analyzed. The average particle size is 160 ± 25 nm. Figure 2.16b shows the SEM micrograph of the RESS co-precipitated RDX/VDF-HFP_{22} nanoparticles. The average particle size of the co-precipitated RDX/VDF-HFP_{22} nanoparticles is 101 ± 25 nm.

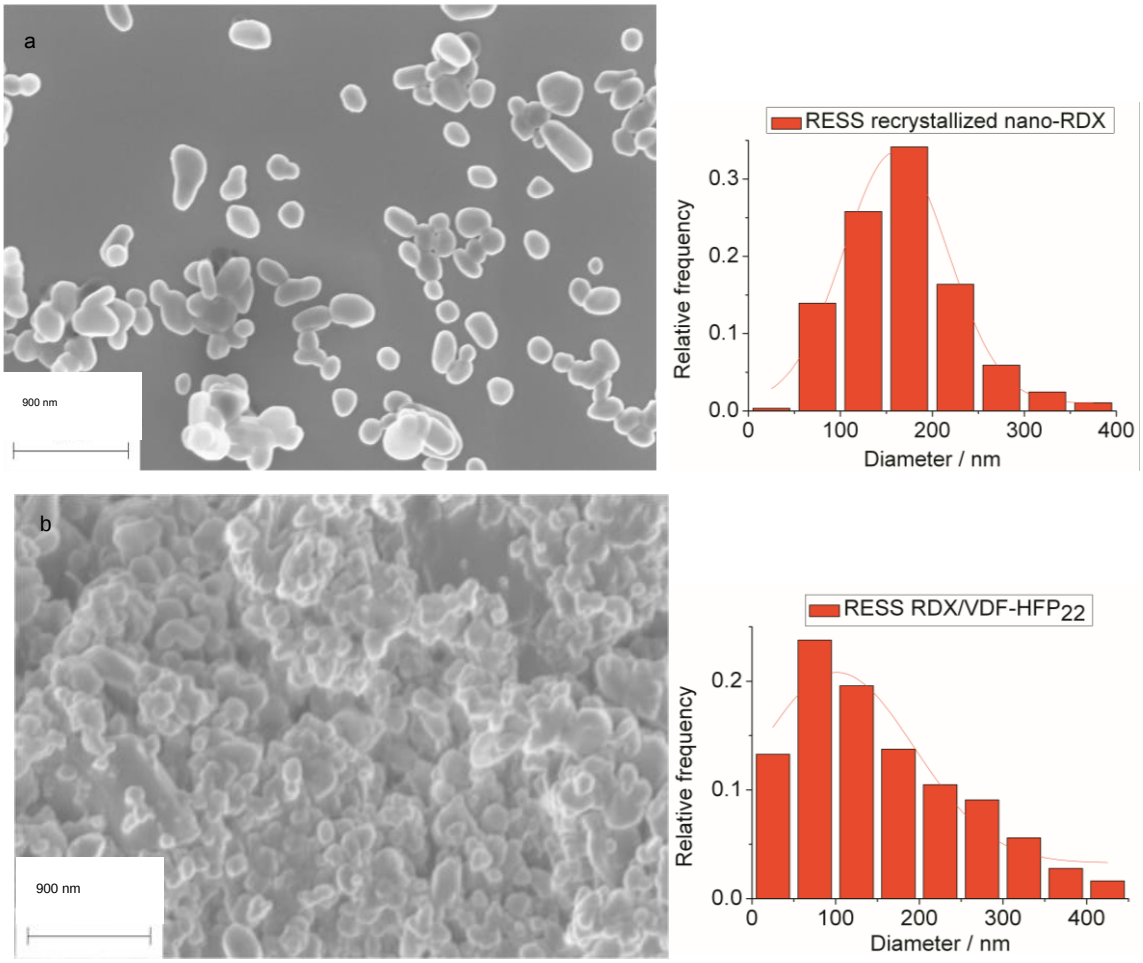

Figure 2.16 SEM micrographs of sample I, RESS recrystallized nano RDX made of 0.16 g RDX at temperature 52 ℃ and pressure 200 bar (a) and sample II, RESS co-precipitated RDX/VDF-HFP_{22} nanoparticles made of 0.16 g RDX and 0.04 g VDF-HFP_{22} polymer at temperature 48 ℃ and pressure 200 bar (b). On the right hand side – the size distribution functions.

Total of 447 particles from three SEM images of the same sample were analyzed. The particles produced by co-precipitation appear to agglomerate more readily, likely due to the presence of VDF-HFP_{22} polymer which has a relatively low glass transition temperature (Tg = -20 ℃). At low glass transition temperatures, nanoparticles tend to agglomerate (46). The absence of individual particles in the images is a result of plasticization of the polymer by CO_2 (46). By comparing the micrographs, it is apparent that the average particle size of RDX/VDF-HFP_{22} is ca. 25-50 nm smaller than that of pure RDX. This could be due to the impeding of the RDX particle growth by the polymer layer.

2.4.6 Transmission Electron Microscopy Analysis

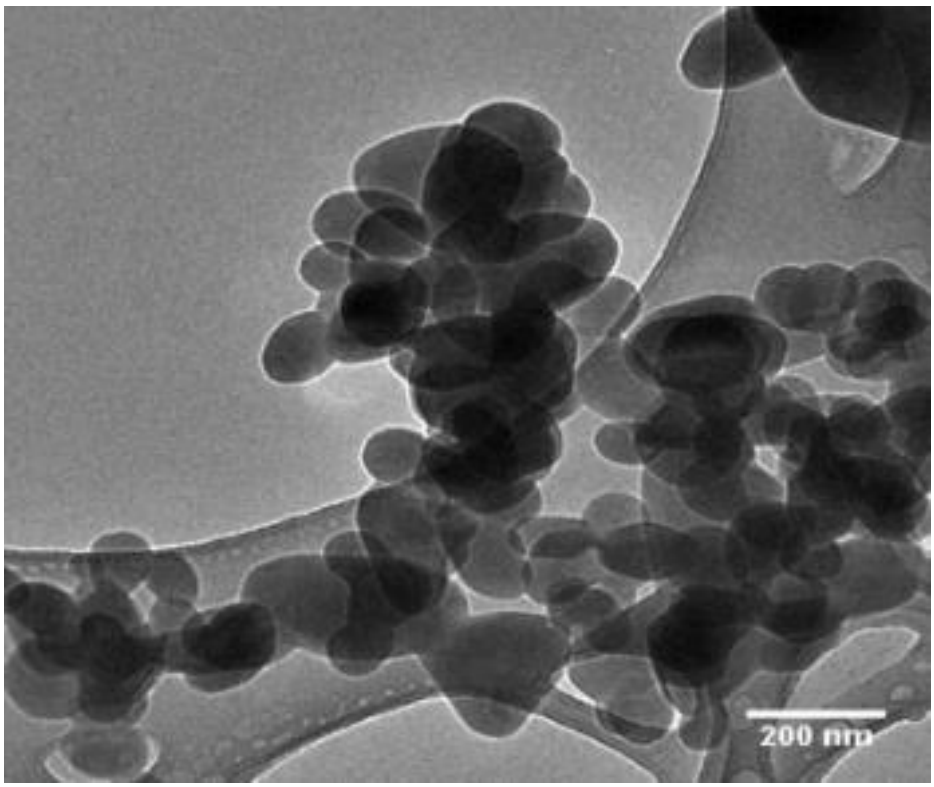

Figure 2.17 TEM micrograph of sample II, RESS co-precipitated RDX/VDF-HFP_{22} nano-composite.

Transmission Electron Microscopy of fabricated specimens was performed with a Philips CM20 cryo-TEM/STEM. Nano-RDX/VDF-HFP_{22} composite (sample II) powder was loaded onto a TEM grid and imaged using TEM under cryogenic conditions. A representative TEM micrograph of sample II RDX/VDF-HFP_{22} nanoparticles (Figure 2.17) demonstrates the particles have near-spherical shape.

The particle size is ca. 100 nm. Here, the distribution of the polymeric binder was not revealed due to the lack of contrast between the polymer and RDX. To circumvent the problem, heavy element staining is commonly employed, typically with RuO_4. Ruthenium tetroxide was introduced as a differential stain. It is used to label aromatic moieties from aliphatic ones. It can react with certain polymers to enhance contrast during TEM imaging. It is a strong oxidizer and has shown penetration depth of 100 nm within 15 min of reaction time (47). However, VDF-HFP_{22} does not react with RuO_4 and, therefore, another polymer must be used for enhanced structural determination of the RESS co-precipitated RDX composites. Polystyrene has been shown to be effectively stained by RuO_4 (48). RuO_4 vapor covalently opens aromatic rings in polystyrene, RuO_2 nanocrystal deposit on polystyrene free surface. As polystyrene continuously exposed to RuO_4 vapor, a continuous film of electrically conductive RuO_2 forms, which reduce the overall contrast that obtained in transmission electron imaging. Therefore, polystyrene was chosen as an alternative to VDF-HFP_{22} in preparation of RDX/binder nanocomposites. The RDX/PS nanocomposite (sample III) prepared by RESS co-precipitation was exposed to ruthenium tetraoxide (RuO_4) vapor (from 1 drop of 0.5 wt. % aqueous

RuO_4 solution) at room temperature for 20 min and then analyzed using cryogenic TEM. The TEM micrographs of sample III RDX/PS nanoparticles with and without RuO_4 vapor treatment are shown in Figure 2.18.

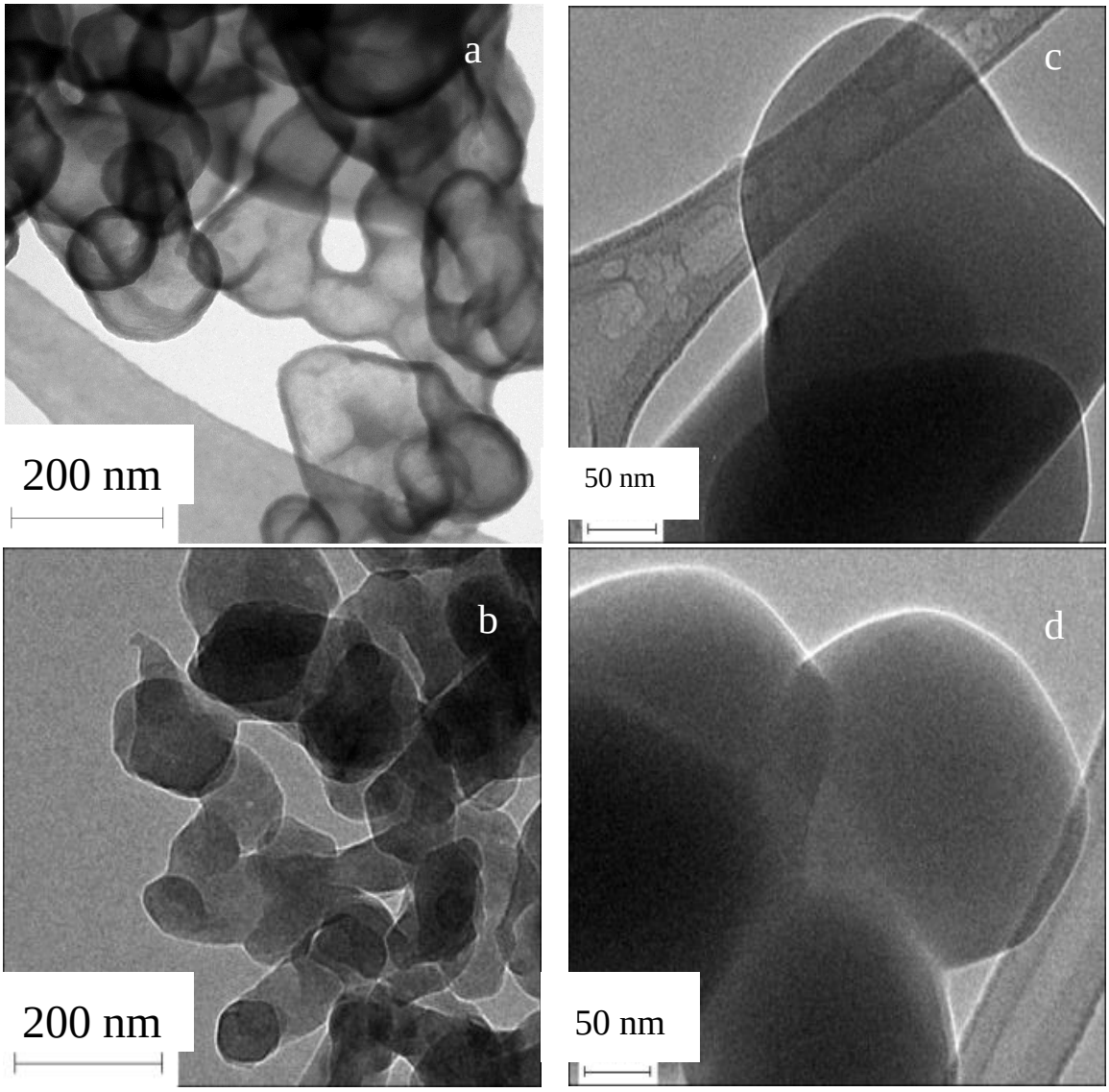

Figure 2.18 TEM micrographs of RESS produced nanoparticles. Two micrographs on the left are the RESS co-precipitated sample III RDX/PS nano-composite (205 bar, 53 ℃): powder stained by RuO_4 (a) and without staining (b). Two micrographs on the right are RESS recrystallized sample I nano-RDX (200 bar, 52 ℃): powder stained by RuO_4 (c) and without staining (d).

RuO_4 staining was very effective for enhancement of the contrast between

RDX and PS. The thin layer visible around the particles corresponds to the stained polystyrene. The TEM image (Figure 2.18a) clearly shows that the polystyrene layer completely covers the RDX core. The thickness of the dark PS coating is estimated as ca. 8 nm. Estimated weight fraction of the polymer from the film thickness is 30 ± 7% (which corresponds to the RDX weight fraction of 70 ± 7%), in excellent agreement with the GC-MS and XRPD determinations. From this analysis it can be concluded that a core/shell structure with RDX at the core is formed. In order to rule out the possibility of the dark layers shown in Figure 2.18a being solely due to the RuO_4 deposition, binder free RDX nanoparticles (Sample I) were treated similarly by RuO_4 vapor. After such treatment, no such layer is visible in the TEM images when no polymer is present (Figure 2.18c). The particles appearance is identical to that of RDX particles untreated by RuO_4 (Figure 2.18d). This further confirms that the dark shells in the particle images shown in Figure 2.18a are composed of polystyrene

Comparison of the TEM micrographs (Figure 2.18a) of stained RDX/PS nanocomposite particles and nano-particles of RDX indicates that PS evenly encapsulates the core. The average size of the RDX/PS nanocomposite particle is ca. 150 nm. Samples of TEM images of stained RDX/PS produced at different pressures are shown in Figure 2.19. The coating layer is resolved for samples made at different pressures. The core-shell structure was stable and not influenced by the process conditions.

2.4.7 Electron Energy Loss Spectroscopy in Transmission Electron Microscopy (TEM-EELS)

TEM-EELS is a powerful tool to analyze microstructures; it can reveal morphologies of different chemical elements contained in a microscopic object. In the RDX/VDF-HFP_{22} nano-composites, only RDX contains element oxygen, while only the polymer (VDF-HFP_{22}) contains element fluorine.

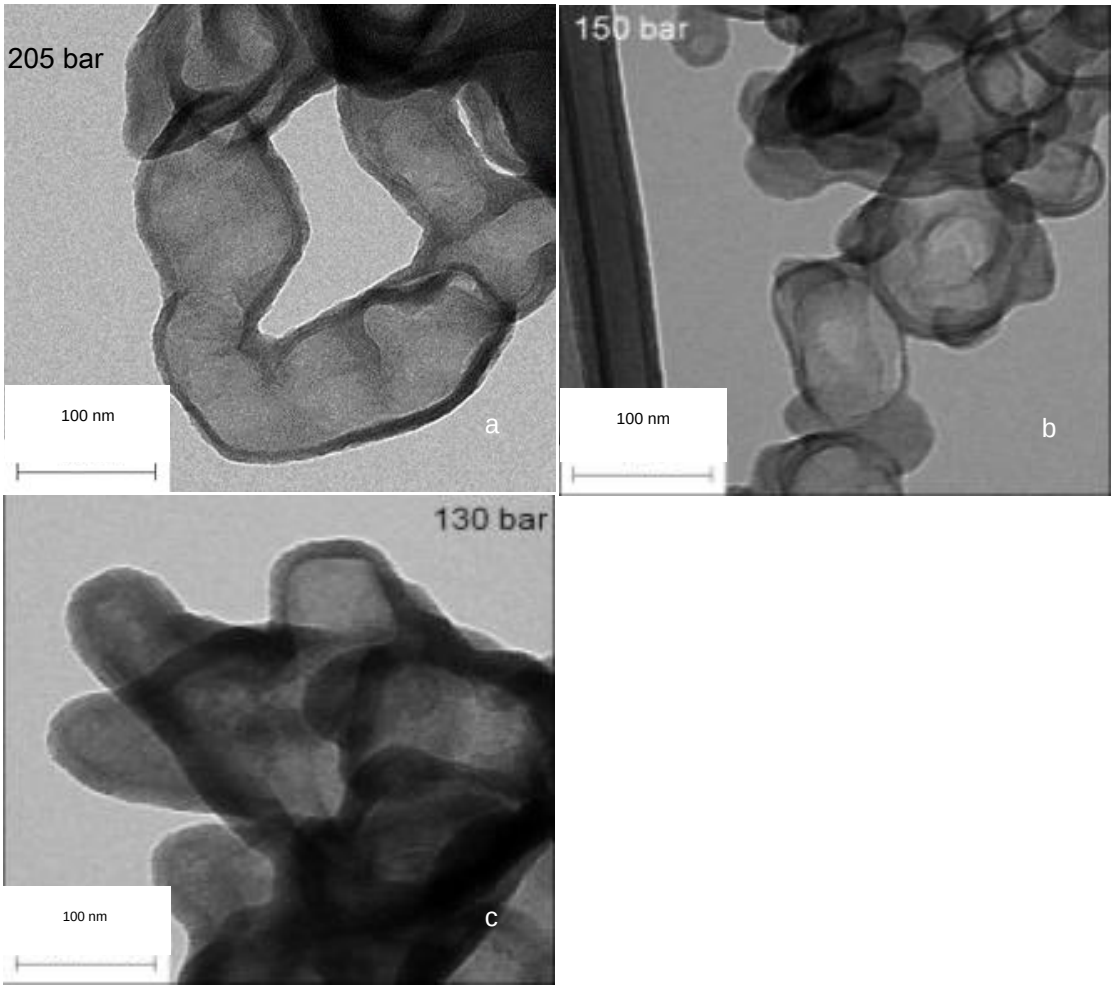

Figure 2.19 TEM micrographs of RESS co-precipitated RDX/PS nano-composite stained by RuO_4. a) sample III prepared at 205 bar, 53 ℃. b) sample IV prepared at 150 bar, 50 ℃. c) sample V prepared at 130 bar, 51 ℃.

The Zero-loss micrograph of the agglomerate of the VDF-HFP_{22} coated RDX nanoparticles is shown in Figure 2.20a, the micrograph of oxygen mapping (RDX only) of the same sample is shown in Figure 2.20b. The size of the coated

RDX/VDF-HFP_{22} particles is estimated as *ca.* 50 nm from the zero loss micrograph. The oxygen mapping (Figure 2.20b) exhibits the same shape and morphology of the RDX nanoparticle agglomerate as the TEM Zero-Loss micrograph (Figure 2.20a). However, the particles are smaller.

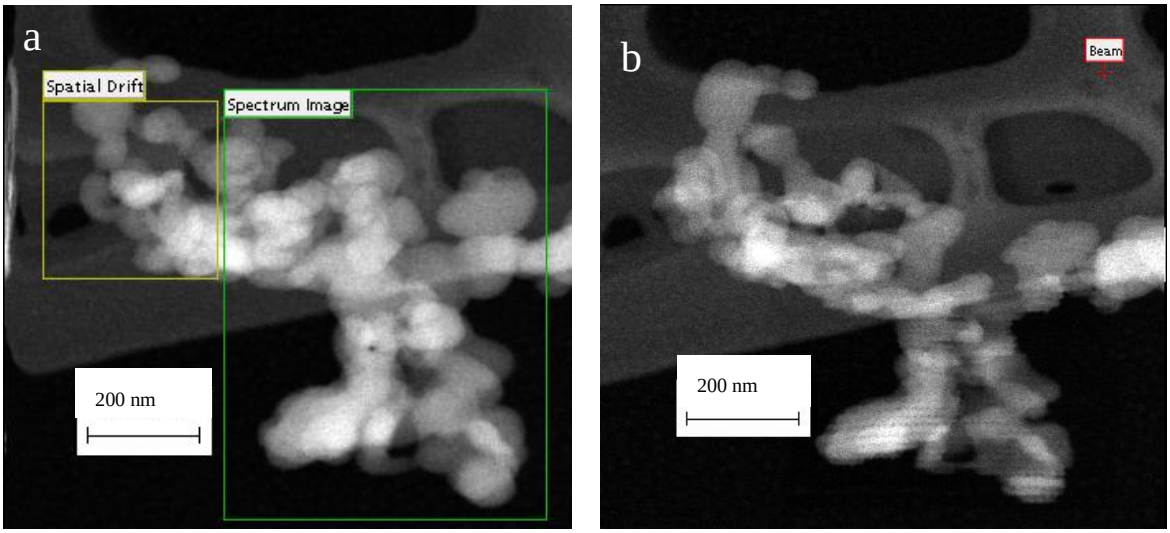

Figure 2.20 TEM-EELS micrographs of RESS co-precipitated RDX/VDF-HFP_{22} nano-composite. (a) zero loss; (b) oxygen mapping.

By comparing the Zero-loss and oxygen mapping micrographs, it is apparent that there is a thin layer of VDF-HFP_{22} covered outside of the RDX nanoparticles. In Figure 2.20a, the part inside the small square labelled "spatial drift" was used as reference for the software to automatically adjust for the drift during the collection of the spectrum; the part inside the "spectrum image" is the area chosen to acquire a higher spatial resolution spectrum. This area is sampled as an array of 160 × 40 points, and each point yields one EELS spectra. The whole sample spectrum and the elemental composition map were extracted based on the spectrum image. By roughly estimating the area of the nano-composite and RDX, there is 82% area of RDX inside

the composite area. Estimating the particle diameter as 100 nm, this leads to the coating layer thickness of 5 nm, in fair agreement with the thickness obtained by staining procedure (9 nm).

CHAPTER 3

CO-PRECIPITATION OF IBUPROFEN AND POLYMERS COMPOSITE BY RESS

3.1 Materials

Ibuprofen (98+%, GC grade) was purchased from Sigma-Aldrich. Poly (L-lactic acid) (MW 50,000 g/mol) was purchased from Polyscience Inc. Poly (lactic-co-glycolic acid) (LA:GA 60:40, MW 4,000 g/mol) was purchased from Polyscitech Inc. Polyethylene glycol (MW 20,000 g/mol) was purchased from Fluka. Common organic solvents were used as purchased. Ethanol (99.9%, HPLC grade) was purchased from Sigma-Aldrich. Dichloromethane (99.9%, HPLC grade) was purchased from Sigma-Aldrich. Carbon dioxide (99.8+%, bone dry grade) pressurized with helium was purchased from Airgas.

3.2 Results and Discussion

3.2.1 Optical Microscopy

RESS recrystallized ibuprofen particles and co-precipitated ibuprofen/polymer particles were characterized using optical microscope equipped with an ICCD camera. Sample images of particles produced at 140 bar and 56 ℃ are shown in Figure 3.1.

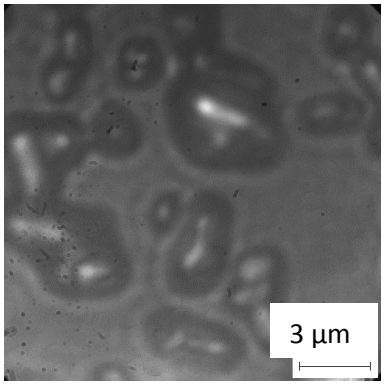	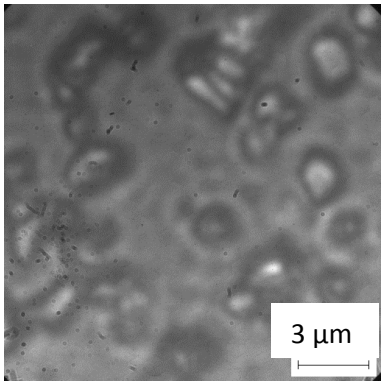	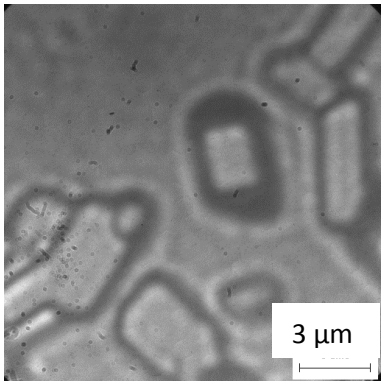
a. RESS ibuprofen	b. RESS PLLA	c. RESS ibuprofen/PLLA
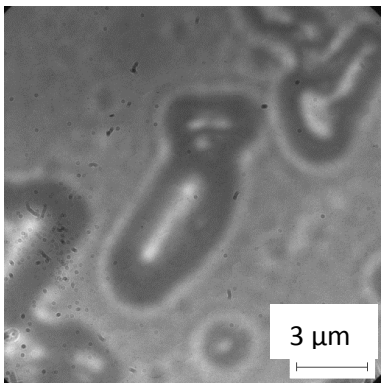	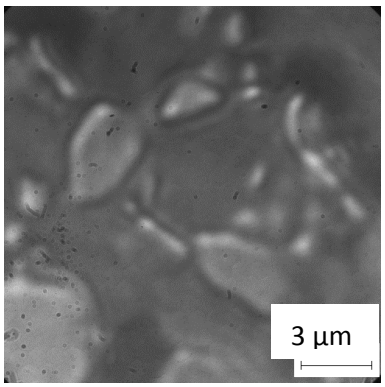	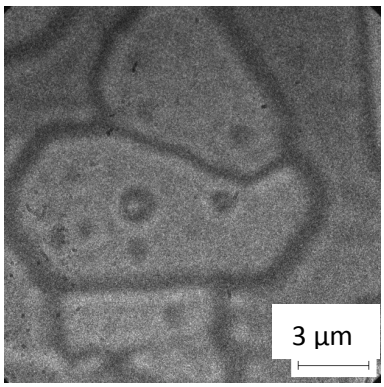
d. RESS ibuprofen	e. RESS PLGA	f. RESS ibuprofen/PLGA
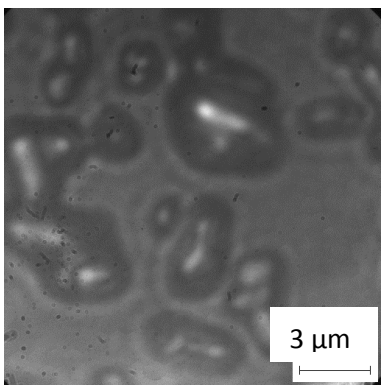	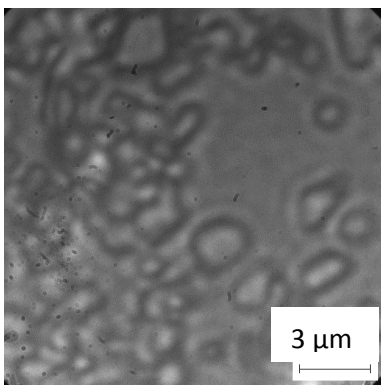	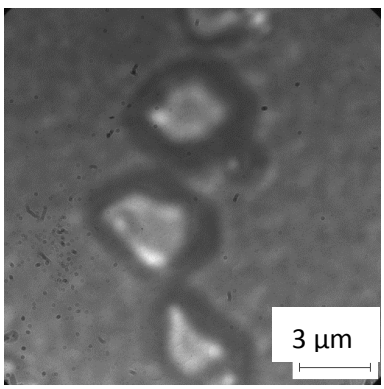
g. RESS ibuprofen	h. RESS PEG	i. RESS ibuprofen/PEG

Figure 3.1 Optical microscopy images of pure RESS ibuprofen (a, d, g) particles pure RESS polymer particles (b, e, h) and RESS co-precipitated ibuprofen/PLLA, ibuprofen/PLGA, ibuprofen/PEG composite particles (c, f, i).

In this run, ibuprofen and the polymer were loaded to the respective extraction vessels with the mass ratio of 1:4. The co-precipitated particles are larger than the particles produced in expansion of supercritical solutions containing single components. Amorphous polymer PLGA has lower molecular weight compared to PLLA and PEG, which are semi crystallized polymers, respectively. As it was found, at the conditions used in this work the concentration of the SC solutions is governed by the transport phenomena rather than by the solubility of the solutes. Dissolution of polymers is accompanied by the plasticization and swelling caused by the penetration of CO_2 into the polymer （35）. PLGA has lower molecular weight and is amorphous, both factors increasing the rate of penetration of CO_2 molecules (49). This leads to higher concentrations of PLGA in the SC solutions, and, subsequently, to larger particles.

3.2.2 Particle Size Distribution

To evaluate the particle size distribution, 30 images of each sample were randomly captured, containing ca. 300 particles. The distribution functions were obtained by manually measuring each particle area using Image-Pro Plus 6.0 software and calculating their equivalent diameter (according to the equation: $A = \pi(d/2)^2$, where A is the spot area, and d is the equivalent diameter). The size distributions of the ibuprofen particles obtained by RESS re-crystallization at different conditions are shown in Figure 3.2. The average particle size depends on the pre-expansion temperature and pressure. The load of ibuprofen in the extraction vessel also has impact on the particle size.

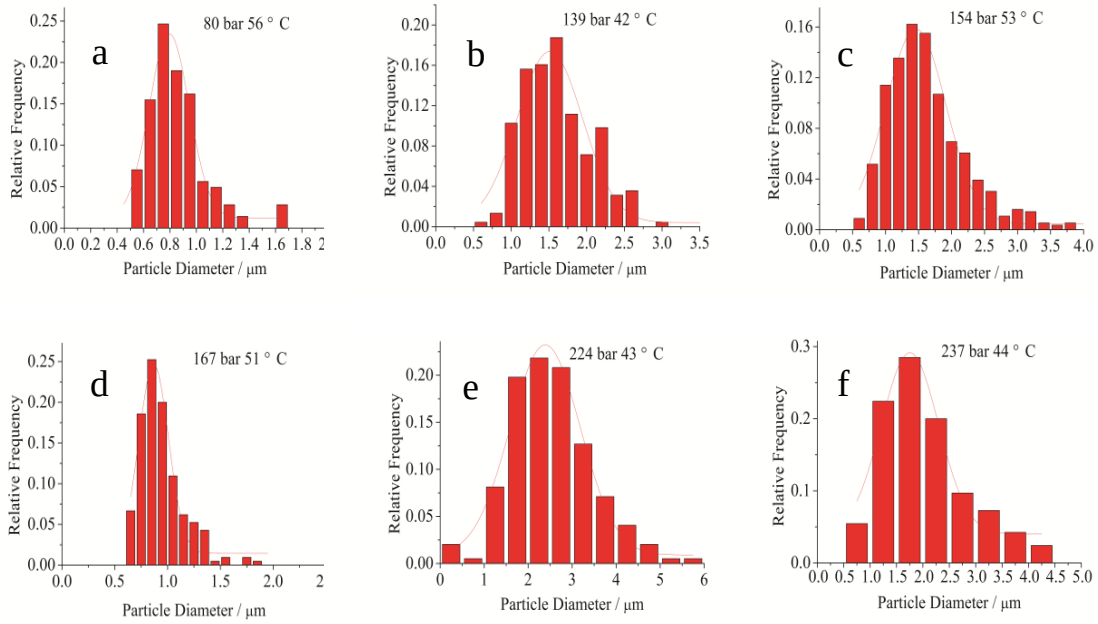

Figure 3.2 The particle size distribution of RESS recrystallized ibuprofen produced at different conditions. a: 80 bar 56 ℃, b: 139 bar 42 ℃, c: 154 bar 53 ℃, d: 167 bar 51 ℃, e: 224 bar 43 ℃, and f: 237 bar 44 ℃.

3.2.3 Kinetics of Dissolution of Produced Powders

Dissolution kinetics of the produced powders was measured at ambient temperature (25.0 ± 0.5 ℃) as well as human body temperature (37.0 ± 0.5 ℃). Weighed samples sieved through a 150 μm mesh were introduced into 500 mL of distilled water. The flask was continuously stirred at 50 rpm using a paddle stirrer. Aliquots (3 mL) were sequentially withdrawn at specific time intervals. After withdrawal of a sample, equal amount of fresh distilled water was added to the solution. The maximum dilution of the solution caused by this sampling procedure did not exceed 12 %. The withdrawn samples were filtered through a 0.22 μm membrane filter (Costar, USA). The amount of ibuprofen in the withdrawn samples was determined by measuring the absorbance at 222 nm wavelength using a UV-VIS spectrophotometer (SHIMADZU Corporation).

Calibration experiments for UV-Vis absorbance at 222 nm were performed on different concentrations of standard ibuprofen solution. A linear regression line was drawn. The extinction coefficient measured using standard solutions of ibuprofen in water is (ε_{10}(222 nm) = (9.04 ± 0.45)x10^3 L mol^{-1} cm^{-1}).

Figure 3.3 shows the temporal profiles of the dissolution of the original material as well as the produced powders at 20 ℃. The dissolution rate coefficient k_w is used as a basis for comparison of the dissolution rates. It is defined as the reciprocal time at which at which 63.2% (1-e^{-1}) of the original amount of the drug is dissolved (50). The dissolution rate coefficient of the RESS micronized ibuprofen is 0.002 min^{-1}, which is two times faster than that of the original material. The micronized ibuprofen agglomerates upon deposition, which leads to a relatively slow dissolution. The ibuprofen composites dissolve much faster than both the original material and the RESS recrystallized pure ibuprofen. This is due to the polymer shell between the drug particles which serves as a protecting layer which efficiently prevents the drug particles from agglomeration. The dissolution rate coefficients of the RESS co-precipitated ibuprofen/PLLA, ibuprofen/PLGA, and ibuprofen/PEG are 0.009 min^{-1}, 0.018 min^{-1}, and 0.02 min^{-1}, respectively. These dissolution rates are respectively nine, eighteen, and twenty times faster than the dissolution rate of the unprocessed ibuprofen. Polymer PLLA is a highly crystalline and poorly soluble in water biopolymer. Ibuprofen processed with PLLA presumably dissolves by diffusion through a thin PLLA layer.

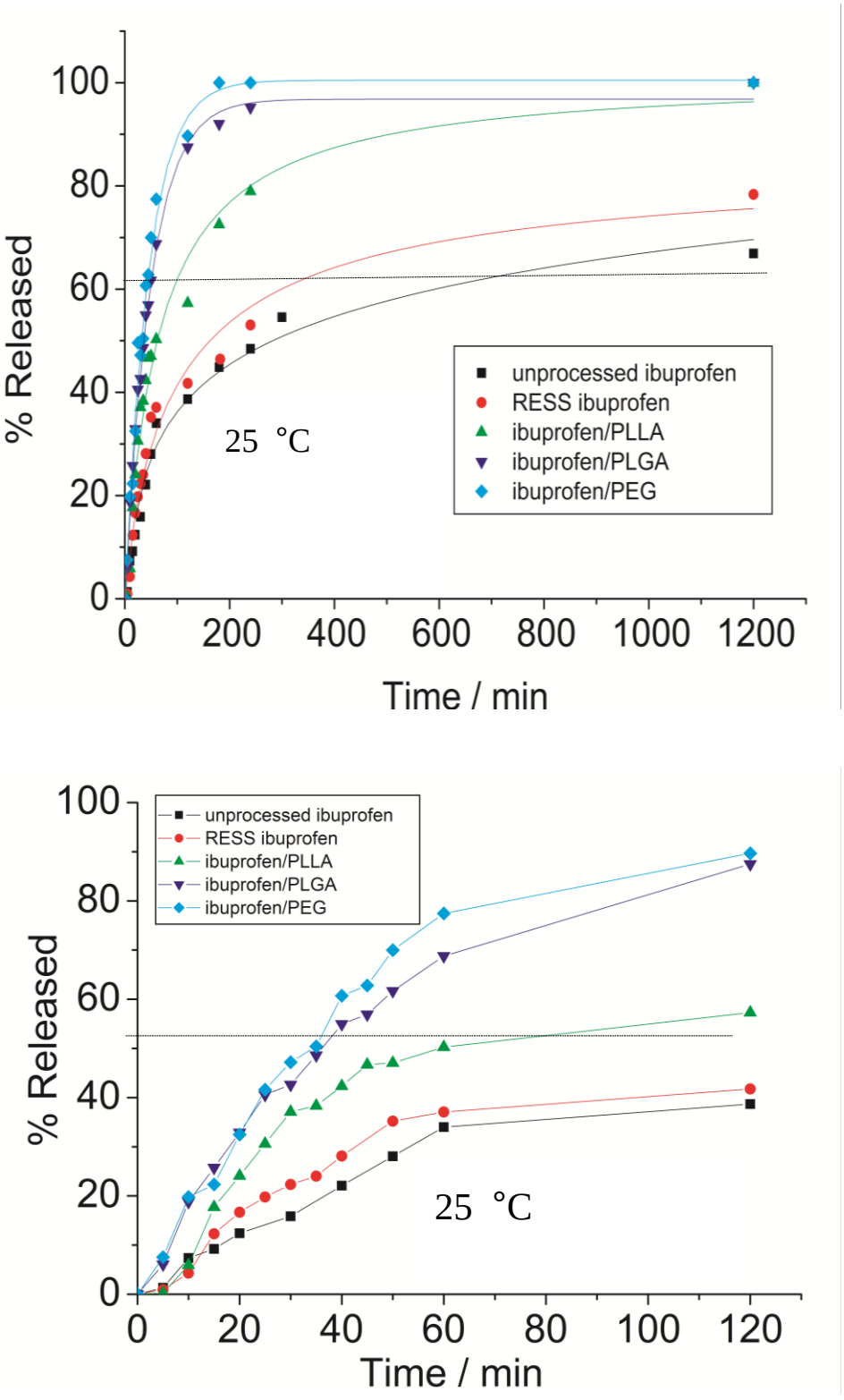

Figure 3.3 Temporal dissolution profiles at 25 ℃. Squares - pure ibuprofen, circles - RESS recrystallized ibuprofen, triangles-up - RESS co-precipitated ibuprofen with PLLA (ibuprofen/PLLA), triangles-down - RESS co-precipitated ibuprofen with PLGA (ibuprofen/PLGA), and diamonds - RESS co-precipitated ibuprofen with PEG (ibuprofen/PEG) (each point is average of three experiments). The horizontal line corresponds to 63.2% of ibuprofen released.

Polymer PEG is a highly water soluble polymer. PLGA dissolved in water undergoes fast degradation caused by hydrolysis of its ester linkages (51). Dissolution of PEG in water is fast (52). Due to the fast degradation or dissolution of the polymeric binders in the ibuprofen/PLGA and ibuprofen/PEG composts, these powders dissolve much faster.

Similar measurements were also performed at the human body temperature 37 ℃. In these experiments, distilled water is still used as the dissolution medium. The results are shown in Figure 3.4. At this temperature the dissolution process is significantly faster than the dissolution process examined at 25 ℃. This is due to the increase of the water solubility of ibuprofen ca. two times compared to the solubility at 20 ℃ (53). The dissolution rate coefficient of unprocessed ibuprofen at 37 ℃ is 0.015 min^{-1}, which is ca. fifteen times larger than at 25 ℃. The dissolution rate coefficient of RESS recrystallized ibuprofen and RESS co-precipitated ibuprofen/PLLA is two times larger than that of unprocessed ibuprofen, and for the RESS co-precipitated ibuprofen/PLGA and ibuprofen/PEG about, three times larger. Ibuprofen co-precipitated with PEG is completely dissolved in 45 min while only 71 % of the unprocessed ibuprofen is dissolved in 120 min. The dissolution rate coefficient is summarized in table 3.1.

Table 3.1 Dissolution Rate Coefficient (k_w) for Unprocessed Ibuprofen, RESS Recrystallized Pure Ibuprofen and RESS Co-precipitated Ibuprofen/PLLA, Ibuprofen/PLGA, and Ibuprofen/PEG

Materials	**Conditions**	**Dissolution T** / ℃	**Dissolution k_w** / min^{-1}
Ibuprofen	(grinded, 150 μm mesh)	25	0.0010
		37	0.015
Ibuprofen,	RESS at 154 bar, 53 ℃,	25	0.0020
RESS produced	150 μm mesh	37	0.031
Ibuprofen/PLLA,	RESS at 148 bar, 55 ℃,	25	0.0090
RESS produced	150 μm mesh	37	0.025
Ibuprofen/PLGA,	RESS at 144 bar, 63 ℃	25	0.018
RESS produced	150 μm mesh	37	0.045
Ibuprofen/PEG,	RESS at 140 bar, 63 ℃	25	0.020
RESS produced	150 μm mesh	37	0.043

The RESS recrystallized ibuprofen released faster than the unprocessed ibuprofen mainly due to the size reduction of the particles. As shown in Figure 3.4, in the first 60 min, it is released faster than the RESS co-precipitated ibuprofen/PLLA. PLLA coated ibuprofen is presumably released by diffusion through the PLLA polymer layer, which hinder dissolution, compared to the dissolution of the pure micronized ibuprofen particles. However, it might be expected, that pure micronized ibuprofen powder contains a fraction of larger agglomerated particles, which would slow down the dissolution at the later stages of the process. PLGA undergoes fast disintegration upon dissolution; PEG is highly soluble in water.

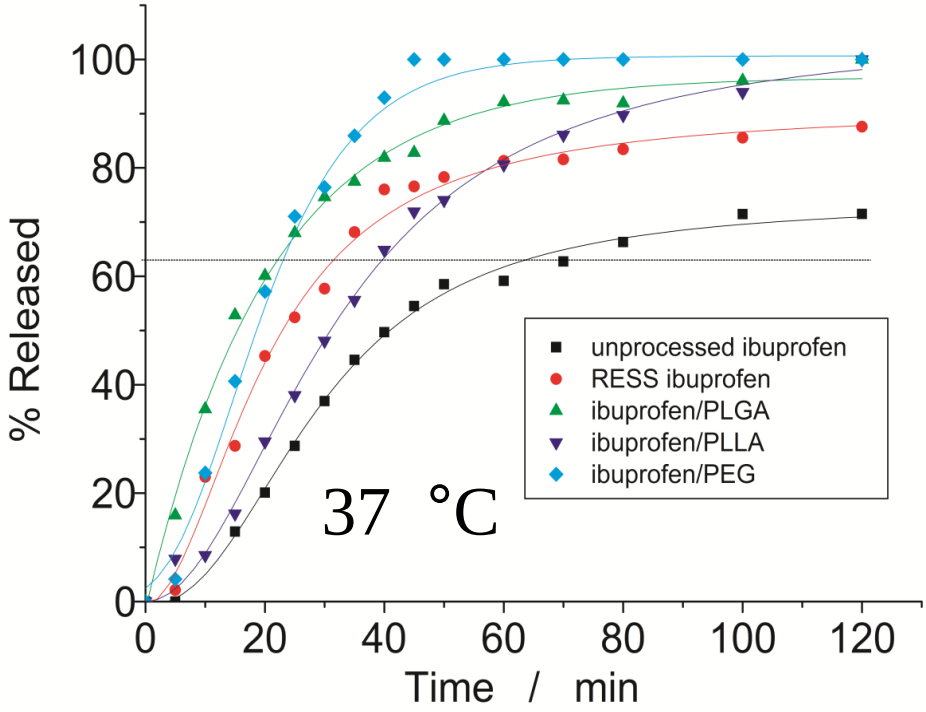

Figure 3.4 Temporal dissolution profiles at 37 ℃. Squares - pure ibuprofen, circles - RESS recrystallized ibuprofen, triangles-up - RESS co-precipitated ibuprofen with PLGA (ibuprofen/PLGA), triangles-down - RESS co-precipitated ibuprofen with PLLA (ibuprofen/PLLA), and diamonds - RESS co-precipitated ibuprofen with PEG (ibuprofen/PEG) (each point is average of three experiments). The horizontal line corresponds to 63.2% of ibuprofen released.

Composites of micronized ibuprofen with these two polymers exhibit higher dissolution rates. PLGA is an amorphous polymer with 60:40 mole ratio of lactide to glycolide randomly blocked monomers. PLGA hydrolysis leads to lactide and glycolide monomers breaking long polymer chains to shorter chains. This facilitates permeation of water towards ibuprofen as well as escape of ibuprofen into the solution. The release of ibuprofen in the case of the ibuprofen/PLGA composite is even faster than the ibuprofen/PEG composites during the initial 30 min of the process, as shown in Figure 3.4. Short induction periods in the dissolution of ibuprofen/polymer composites are apparent (Figure 3.4). The induction periods are

presumably to the dissolution of the polymers which precede release of ibuprofen into the solution.

To check whether UV absorption of dissolved polymers interferes with the ibuprofen absorption at 222 nm, additional experiments on dissolution of pure polymers in water were performed at 37.0 ± 0.5 ℃. The polymers were allowed to dissolve in water when agitated with 50 rpm for 120 min. The dissolved amounts were evaluated by measuring the absorbance at 240 nm (54), 270 nm (51), and 510 nm (55) for PLLA, PLGA, and PEG, respectively. The UV absorbance of the three polymers is summarized in table 3.1.

Table 3.2 Polymer UV Absorbance from Literature

Polymer	**Maximum UV absorption wavelength λ** / nm	**Molar extinction coefficient ε_{10}** / L mol^{-1} cm^{-1}	**Solubility in water at 20 ℃** /mg ml^{-1}	**Comment/ reference**
PLLA	240 nm	not available	insoluble	In chloroform (54)
PLGA	270 nm	not available	insoluble	In phosphate buffer solution (51)
PEG	510 nm	$1.37x10^5$	630 mg/mL	In Dragendorff reagent (55)

In the case of PEG, maximum absorbance at 510 nm was reached at 5 min, with subsequent decline due to the dilution caused by the sample withdrawal procedure. In the case PLGA, no absorbance was detected. The PLGA samples after

the procedure were extracted, dried and weighed. The weight loss was 10%, indicating that this amount of the polymer was left in the solution. However, no absorbance at 270 nm was detected. In the case of PLLA, no weight loss of the sample was detected, confirming that PLLA is not water soluble. Finally, for all three polymers there was no absorbance observed at 222 nm (Figure 3.5).

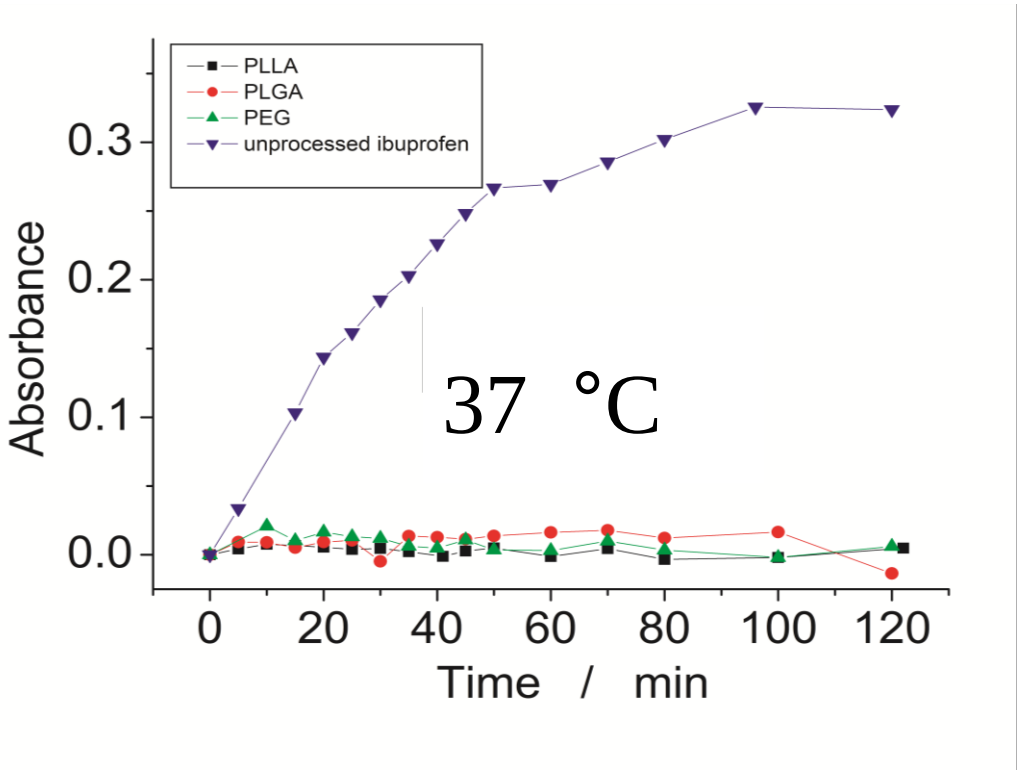

Figure 3.5 Control experiments on the dissolution of pure polymers at 37 ℃ in comparison with the dissolution of unprocessed ibuprofen. Absorbance is measured at 222 nm. Squares - PLLA precursor, circles - PLGA precursor, triangles-up - PEG precursor, and triangles-down - unprocessed ibuprofen.

Ibuprofen is a weak acid. Its dissolution rate could be influenced by the increase of the acidity of the dissolution medium. Therefore, a buffer solution would be required to maintain a constant pH. However, in this study, the dissolution medium used was distilled water. Ibuprofen has pKa of ca. 5. In the experimental procedure,

10 mg of ibuprofen were dissolved in 500 ml of distilled water. The final pH of the solution is 4.4.

Rivera-Leyva (56) et al. studied the dissolution kinetics of commercial ibuprofen suspension. The dissolution rate coefficient in a buffer medium with pH=7.2 is 0.03 min^{-1}, and in a buffer medium with pH=4.5 is 0.02 min^{-1}. In the buffer medium with pH=7.2 ibuprofen was 100% released in 60 min. In the pH=4.5 buffer medium, 90% of ibuprofen was released in 120 min. These measurements demonstrated that the dissolution of ibuprofen is influenced by the acidity of the medium. Although in our experiments the measurements were performed in the conditions of changing pH in the dissolution process, the conclusions on the relative dissolution rate are still valid, since all experiments were performed over the same pH range.

CHAPTER 4

MECHANISM OF PARTICLE FORMATION IN RESS

4.1 Spray-drying Model

Spray-drying is a conventional method widely used to produce small particles. In the spray-drying process, a liquid solution is first broken into millions of droplets which form a spray, this process is called atomization (57). Then the spray contacts with the drying medium, usually a heated air or inert gas, where evaporation occurs.. After that the dried product is collected at the base of the drying chamber. In the spray-drying process, the particle size as well as the particle size distribution is controlled by the droplet size distribution and the solute concentration in the solution.

4.2 Tentative Particle Formation Mechanism

In the previous work it was shown that the particle size of particles precipitated by RESS is significantly larger than the particle size expected due to the homogeneous nucleation and growth of the solute (58). For RDX, the predicted maximum particle size by the homogeneous nucleation and growth model was ca. 20 nm,(REFERENCE) with the observed size of about 200 nm (depending upon the conditions), which translates into the 1000 times discrepancy in the particle mass. For this specific system (RDX precipitation) it was unambiguously shown that the homogeneous precipitation and growth is not the mechanism responsible for the particle formation in the RESS process. Alternatively, a modified spray-drying model was proposed (58). This model is based on the observation that the RESS of SC solutions in CO2 is

accompanied by condensation (with subsequent evaporation) of carbon dioxide. Then the process is equivalent to the spray-drying process which differs mainly by the fact that the condensed phase appears in the stage of the spray formation. Additional feature is the impact of the dissolved solute on the droplet (or crystals) condensation dynamics and the size distribution. The model, in the first approximation, predicts the volume of the solute particles to be proportional to the concentration of the solution, or, alternatively, the diameter to be proportional to the cubic root of the concentration

$$d \sim C^{1/3} \tag{4.1}$$

where d is the diameter of the solute particle formed, and C is the mass concentration of the solute in the supercritical solution.

To verify the particle formation mechanism in the case of ibuprofen precipitation, additional experiments on ibuprofen particles formation by RESS when the concentration of dissolved ibuprofen was systematically varied were carried out. The amounts of the dissolved ibuprofen and the polymers were accurately measured by weighing the extraction vessels before and after each run. It was found that the weight losses did not correspond to the solubility of these compounds in supercritical carbon dioxide, and that the solution was not saturated either with ibuprofen or the polymers. In addition, the weight loss was increasing with the initial load. These observations indicate that the dissolved amounts are controlled mainly by other factors, such as the transport and the dissolution rates.

The main observations of this study were rationalized based on the modified spray-drying mechanism (58).

Upon expansion, the stream of the supercritical solution undergoes fast cooling which leads to the formation of liquid carbon dioxide or, at lower downstream pressures, dry ice. The entrained quantities of the solutes in the droplets are proportional to their concentrations in the supercritical solution. Subsequently, carbon dioxide evaporates or sublimes, leaving solid composite particles consisting of the entrained solutes.

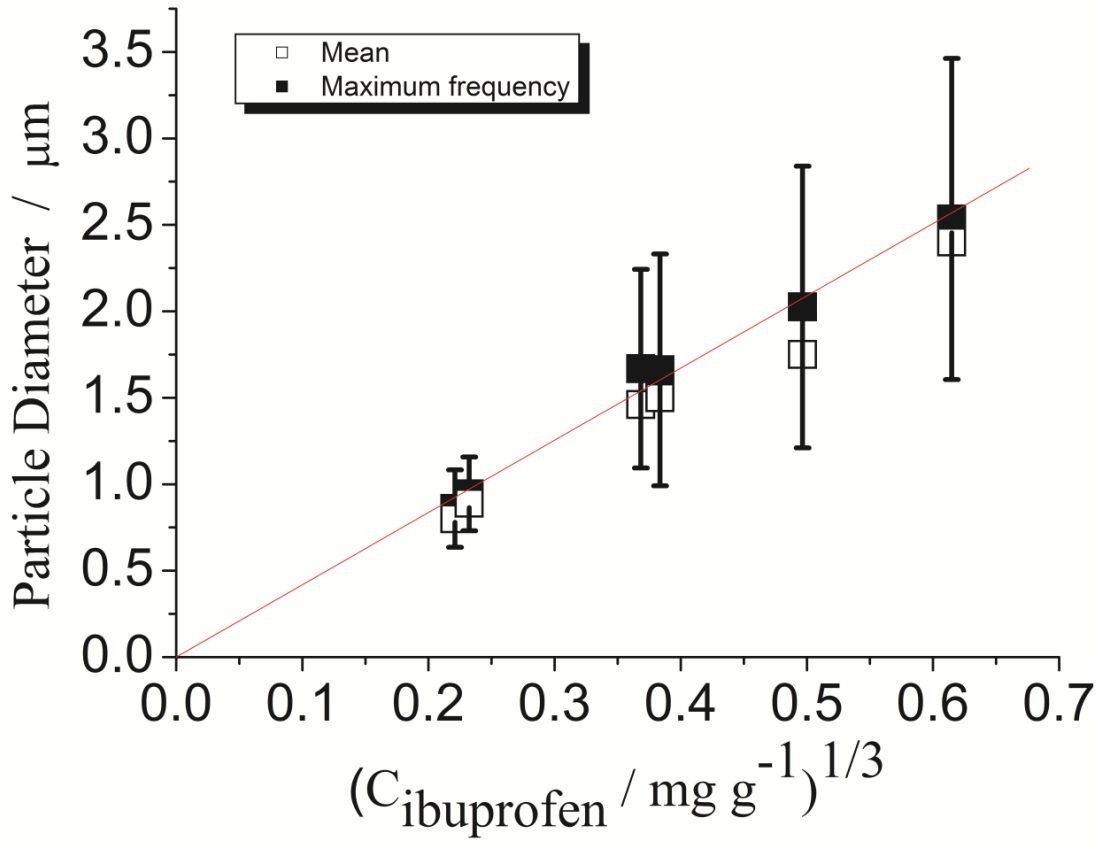

Figure 4.1 The particle size distribution of RESS recrystallized ibuprofen produced at different conditions. a: 80 bar 56 ℃, b: 139 bar 42 ℃, c: 154 bar 53 ℃, d: 167 bar 51 ℃, e: 224 bar 43 ℃, and f: 237 bar 44 ℃. Filled squares are the mean diameter, open squares are the diameters in the maxima of the distribution functions, and the error bars are ±1standard deviation.

To check the particle size dependence on the solution concentration predicted by the modified spray-drying mechanism (4.1) recrystallization of ibuprofen by RESS was conducted at different conditions. Concentration of ibuprofen in the supercritical solutions was varied by varying the load and pressure. Figure 4.1 shows the plot of the average particle size vs. the cubic root of the solution concentration. The measured dependence is linear and goes through the origin which is in accord with the suggested mechanism.

CHAPTER 5

SOLUBILITY OF COMPOUNDS IN SUPERCRITICAL CARBON DIOXIDE

5.1 Polymer Dissolution in Liquid Solvent

The process of polymer dissolution differs significantly from the process of dissolution of material made of small size small molecules. For non-polymeric materials, the rate of the "external" mass transfer controls the rate of the dissolution process. For polymers, the dissolution rate is usually controlled either by the solvent diffusion or the disentanglement of the polymer chains (59). As a result, polymers do not dissolve "instantaneously".

Crank (60) summarized the structure of the glassy polymers during dissolution above its gel temperature.

1. The infiltration layer: the solvent molecules penetrate into the polymer free volumes.

2. The solid swollen layer: more and more solvent penetrate into the polymer, new holes created but the polymer is still in the glassy state.

3. The gel layer: as the polymer becomes swollen by the solvent molecules, it is in the rubber-like state.

4. The liquid layer: this layer surrounds the internal undissolved solid layers.

For dissolution below a certain temperature, the gel layer is not formed. Instead extensive cracking inside the polymer matrix occurs which facilitates the solvent penetration. This specific temperature is defined as the gel temperature of the

polymer. Therefore, the variation in the free volume and the stiffness of the polymer play an important role for controlling the polymer behavior

Higher molecular weight polymers dissolve slower because they have higher degree of chain entanglement which will make the swelling process much longer than that for the lower molecular weight polymers. Also they are packed more densely with less pores and cracks or other kind of imperfections (49), which slow down the solvent diffusion process.

From the thermodynamic view, the dissolution of a polymer in a solvent is governed by the free energy of mixing (61):

$$\Delta G_m = \Delta H_m - T\Delta S_m \tag{5.1}$$

where ΔG_m is the molar Gibbs free energy of mixing, ΔH_m is the enthalpy of mixing, T is the absolute temperature, and ΔS_m is the entropy of mixing. Since the dissolution of polymers is usually accompanied with a small positive entropy change, the enthalpy change becomes the controlling factor. The enthalpy of mixing is given by

$$\Delta H_m = V_{mix} [(\Delta E^v_1/V_1)^{1/2} - (\Delta E^v_2/V_2)^{1/2}]^2 \Phi_1 \Phi_2 \tag{5.2}$$

where V_{mix} is the volume of the mixture, ΔE^V_i is the energy of vaporization of species i; V_i is the molar volume of species i; and Φ_i is the volume fraction of i in the mixture.

The Hildebrand solubility parameter δ is defined as (59)

$$\delta = (E/V)^{1/2} \tag{5.3}$$

where E is defined as the increase in the internal energy per mole of the material if in the process of elimination of all of the intermolecular forces E is also called the the cohesive energy. V is the volume of the material per mole, E/V is the cohesive energy density. Parameter δ has the same meaning as the term $(\Delta E^{v}_{i}/V_{i})^{1/2}$ in Equation 5.2. Therefore, the enthalpy of mixing can be rewritten as:

$$\Delta H_m = V_{mix} [(\delta_1 - \delta_2)]^2 \Phi_1 \Phi_2 \tag{5.4}$$

In order to the dissolution process to occur spontaneously, the Gibbs free energy of mixing must be negative. Therefore the ΔH_m term should be smaller than the $T\Delta S_m$ term in Equation 5.1. From Equation 5.4, to make ΔH_m small, $\delta_1 - \delta_2$ should be as small as possible. It means that the solubility parameter difference between the solute and solvent should be small in order to make the solute readily dissolved in the solvent. This principle is also known as ‘like dissolves like’.

Table 5.1 Solubility Parameter Calculations of RDX and Binders

Chemical	**Atoms & groups**	**ΔE_v** cal/mol	**V** cm^3/mol	**δ** $(cal/cm^3)^{1/2}$
RDX	3 NO_2	1.519×10^4	137.8	10.49
	3 CH_2			
	3N			
	6 member ring			
VDF-HFP_{22}	5 CF_2	1.219×10^4	255.7	6.910
	4 CH_2			
	1 CF_3			
	1 C			
	1 F			
	10 main chain			
PS	1 CH	9.630×10^3	94.50	10.10
	1 CH_2			
	1 C=			
	5 CH=			
	3 conjugated double bonds			
	1 6-member ring			
AMC	6 member ring	3.901×10^4	315.9	11.11
	CH_3			
	NH_2			
	CO			
	O			
	CH=			
	C=			
	4 conjugated			

Fedors et al. (62) developed the group contribution method to estimate the solubility parameters δ:

$$\delta=\left(\frac{\Delta \mathrm{Ev}}{\mathrm{v}}\right)^{1/2}=\left(\frac{\sum_i \Delta ei}{\sum_i \Delta vi}\right)^{1/2} \tag{5.5}$$

Δe_i is atomic and group contributions to the energy of vaporization per mole, and Δv_i is the atomic and group contributions to the molar volume at a specific temperature. At room temperature, δ_{CO_2} equals 5.96 (61) and δ_{RDX} equals 10.49 (7). The calculated solubility parameter at room temperature of the chemicals used in this work, which was listed in Table 3. We find that VDF-HFP_{22} is the most favored in CO_2.

5.2 Polymer Dissolution in Carbon Dioxide

The polymer dissolution in supercritical carbon dioxide will include several steps (63) as shown in Figure 5.1:

1. CO_2 molecule absorb on the surface of the polymer.CO_2 molecule diffuses into the polymer matrix.
2. CO_2 concentration inside the polymer reaches a critical concentration where the polymer chains have enough space to disentangle from each other and start to dissolve into the solvent. The dissolution rate is low, the process is still CO_2 adsorption/absorption controlled.
3. The polymer dissolution rate increases to be higher than the CO_2 adsorption/absorption rate. The polymer dissolution occurs much faster, the process become polymer dissolution controlled.

   For most polymers, its solubility in supercritical carbon dioxide increases dramatically and non-linearly as the pressure increased. This is because at higher pressure the density of carbon dioxide is much higher. The solubility of polymers

in CO2 drops sharply as a function of molecular weight. However, complete dissolution of the polymer film is normally not achieved. The non-soluble part may due to having a high molecular weight or a high degree of entanglement.

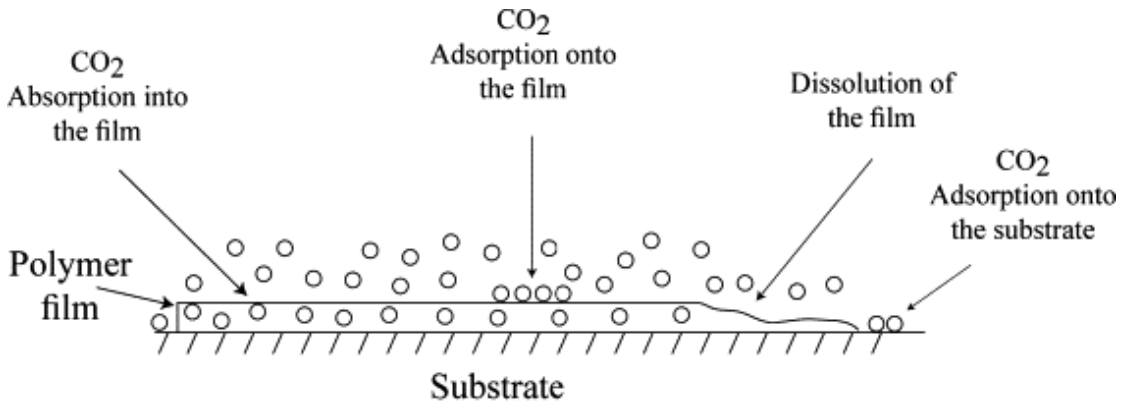

Figure 5.1 Schematic showing the difference phenomena involved during the dissolution process of polymer films (63).

5.2.1 Factors that Influence Polymer Solubility in Supercritical Carbon Dioxide

From lattice solution theory, three factors may influence polymer solubility in supercritical carbon dioxide, which are solute-solute interactions, solute-solvent interactions, and solvent-solvent interactions. CO_2-CO_2 interaction is negligible as compared to the other two factors. A difference in the solubility parameter between a polymer and carbon dioxide would be a representative factor for solute-solvent interaction. O'Neil (64) stated that the surface tension of the polymer is a reliable measurement of cohesive energy density for the polymer-polymer interactions. From the cloud point measurement, it is concluded that polymers solubility in carbon dioxide at temperatures below 80 ℃ is inversely proportional to the surface tension of the polymer, which demonstrated that the solubility is governed primarily by the polymer-polymer interactions. The polymer-CO_2 interactions play a secondary role.

The free volume inside the polymer is also an important factor that influences the polymer solubility in supercritical carbon dioxide (65). It is known, that glassy polymers have lower solubility and dissolution rate compared to completely amorphous polymers (65). The polymers which were used to produce composites with ibuprofen have different crystallinity: PLLA has crystallinity 37% (66), PEG and PLGA are amorphous. This explains the trend in the particle size of these polymers when crystallized by RESS separately.

5.2.2 Polymer Solubility in Supercritical Carbon Dioxide

Rindfleish (65) experimentally tested cloud-point data of polymers and copolymers in supercritical CO_2 up to 27 ℃ and 3000 bar. The solubility of PS (MW 1850 g/mol) is low and below the sensitivity (0.1 wt %) of the cloud-point technique. At 70 ℃, VDF-HFP_{22} has cloud-point pressure of 700 bar. At higher temperatures, the cloud-point pressures are even higher. VDF-HFP_{22} is relatively more soluble than PS in CO_2 because of its fluorine content and the copolymer block in the chain. Also, PS has a T_g of 103 ℃, which indicates that PS has a stiffer chain backbone and have less rotational flexibility of the chain segments. This results in a higher entropy penalty for CO_2 to dissolve PS.

Fluorinating a hydrocarbon polymer improves its solubility in CO_2, because the carbon atom in CO_2 and the fluorine atom in the polymer repeating unit form a weak complex C-F at low temperatures (67). CO_2 can act as an electron acceptor to form Lewis acid-base complexes with polymers that possess electron donating groups, such as fluorine atoms. The hexafluoro propylene (HFP) comonomer disrupts the

stereo regularity of -VDF and thus renders it amorphous. Vinylidene fluoride (VDF) co-monomer introduces polarity into the backbone of VDF-HFP_{22}. Dipole of –VDF interacts favorably with the quadrupole of CO_2, which overshadows CO_2-CO_2 quadrupolar interactions. VDF-HFP_{22} can dissolve in CO_2 at modest pressures and temperatures as low as 0 ℃ due to the dominance of the polar interactions at low temperatures. O'Neil (64) *et al.* experimentally measured the solubility of PS at 207 bar, and 35 ℃, The low molecular weight PS (MW 500 g/mol) is slightly soluble (« 0.1 wt %). However, the PS with MW of 1850 g/mol is "insoluble" in supercritical CO_2. Then the PS used in the current experiments with the MW of 250000 g/mol should be considered as insoluble in CO_2 under the same conditions. As mentioned in our previous work (1), RDX is slightly soluble (0.2 wt %) in CO_2 at 35 ℃, 200 bar.

The solubility can be also discussed based on the solubility parameter δ /(cal / $cm^3)^{1/2}$ (62). At 25 ℃, δ (CO_2) is 5.96, δ (RDX) is 10.49 (7) and δ (PS) (density of 1.06 g / cm^3) is 9.10 (68). Based on the group contribution method as shown in Table 5.1., δ (VDF-HFP_{22}) is calculated as 6.91. VDF-HFP_{22} has the closest δ value to CO_2, as compared to RDX and PS, which means it is more favorable in CO_2 at 25 ℃. This is in accord with the cloud point measurements. The solubility in CO_2 can be arranged from high to low as VDF-HFP_{22} > RDX > PS.

CHAPTER 6

CONCLUSIONS

The technique of production of composite nano- and micron sized materials using Rapid Expansion of Binary Supercritical Solutions was explored and characterized. The technique was applied to two systems: production of nanocrystalline polymer coated energetic materials and micron sized drug – biocompatible polymer composites. The specific results are:

Nanoparticles of RDX coated with PS or VDF-HFP_{22} polymer films were produced by co-precipitation in rapid expansion of supercritical solutions (RESS). The morphology of produced nanoparticles was characterized by SEM and TEM. The size of produced RDX nanoparticles is *ca.* 100 nm. The X-ray powder diffraction indicates that the particles are polycrystalline with crystallite size of 42 nm (similar to the crystallite size for pure nano-RDX, 44 nm). However, RDX diffraction indicates much larger internal strain of the particles. The RDX mass fraction in the produced powders was in the range 70-82%, as analyzed using GC-MS and XRPD. TEM analysis of the RDX/PS nanocomposites assisted by selective staining of the polymer phase showed *ca.* 10 nm shell layer of polystyrene on the RDX core. The observations indicate core-shell structure of the products rather than separate precipitation of the components. RDX was also co-precipitated with AMC, a fluorescent dye compound for evaluation using optical fluorescence microscopy with evanescent excitation.

Comparison of the usual optical images and the images acquired via fluorescence indicates that all produced particles contain the fluorescent dye. No RDX nanoparticles free of dye have been observed.

Micro-particles composite of ibuprofen with bio-compatible polymers were also produced by co-precipitation in rapid expansion of supercritical solutions (RESS). The morphology of produced nanoparticles was characterized by optical microscopy. The size of produced particles is 3-10 microns. Although RESS of pure materials produces nano- or micron-sized particles, there are no means to prevent their agglomeration. Reduction of the size of particles of energetic materials leads to reduction of their sensitivity to external stimuli (38). Micronization of drug particles enhances their bioavailability and the dissolution rate. Co-precipitation of a drug and bioavailable polymers composites can either accelerate or slow down the drug release depending on the chosen polymer. Kilogram to 100 kg level quantities can be produced. The particles size is controlled by varying the experimental conditions (e.g., pressure, load). RESS co-precipitation is a simple one step process. It could be binary or multi-component production. It is environmental friendly, organic solvent free, clean and economic.

The product was evaluated with SEM, TEM, XRD, and GC-MS. Core-shell structure of RESS co-precipitated RDX/PS was demonstrated. It will reduce agglomeration of the particles and enhance functionality. The dissolution profile was examined on RESS co-precipitated ibuprofen and polymers. Remarkable dissolution enhancement was achieved by the co-precipitated composite as compared to

unprocessed ibuprofen. The approach can be extended to other energetic or drug materials with a wide field of applications.

REFERENCES

1. Stepanov V, Krasnoperov L N, Elkina I B, Zhang X. Production of nanocrystalline RDX by rapid expansion of supercritical solutions. Propell Explos Pyrot. 2005;30:178-83.

2. Matson D W, Fulton J L, Petersen R C, Smith R. D. Rapid expansion of supercritical fluid solutions: solute formation of powders, thin films, and fibers. Ind Eng Chem Res. 1987;26:2298-306.

3. Tom J W, Debenedetti P. G. Formation of bioerodible polymeric microspheres and microparticles by rapid expansion of supercritical solutions. Biotechnol Prog. 1991;7:403-11.

4. Domingo C, Berends E, Rosmalen G. M. V. Precipitation of ultrafine organic crystals from the rapid expansion of supercritical solutions over a capillary and a frit nozzle. J Supercri Fluid. 1997;10:39-55.

5. Charoenchaitrakool M, Dehghani F, Foster N. R. Micronization by rapid expansion of supercritical solutions to enhance the dissolution rates of poorly water-solule pharmaceuticals. Ind Eng Chem Res. 2000;39:4794-802.

6. Turk M, Hils P, Helfgen B, Schaber K, Martin H J, Wahl M. A. Micronization of pharmaceutical substances by the rapid expansion of supercritical solutions (RESS): a promising method to improve bioavailability of poorly soluble pharmaceutical agents. Journal of Supercritical Fluids. 2002;22:75-84.

7. Lee B M, Kim D S, Lee Y H, Lee B C, Kim H S, Kim H, et al. Preparation of submicron-sized RDX particles by rapid expansion of solution using compressed liquid dimethyl ether. J Supercrit Fluids. 2011;57:251-8. Epub Mar. 12, 2011.

8. Debenedetti P. G. Homogeneous nucleation in supercritical fluids. AIChE J. 1990;36:1289-98.

9. Chesnokov E N, Krasnoperov L. N. Complete thermodynamically consistent kinetic model of particle nucleation and growth: numerical study of the applicability of the classical theory of homogeneous nucleation. J Chem Phys. 2007;126:144504.

10. Aresta M. Carbon dioxide recovery and utilization. Norwell, MA: Kluwer Academic; 2003. 126 p.

11. Gallagher P M, Coffey M P, Krukonis V. J. Gas anti-solvent recrystallization of RDX: formation of ultra-fine particles of difficult-to-comminute explosive. J Supercrit Fluids. 1992;5:130-42.

12. Falk R, Randolph T W, Meyer J D, Kelly R M, Manning M. C. Controlled release of ionic compounds from poly (L-lactide) microspheres produced by precipitation with a compressed antisolvent. J Control Release. 1997;44:77-85.

13. Pfeffer R, Dave R N, Wei D, Ramlakan M. Synthesis of engineered particulates with tailored properties using dry particle coating. Powder Technol. 2001;117:40-67.

14. Stepanov V, Willey T M, Ilavsky J, Gelb J, Qiu H. Structural characterization of RDX-based explosive nanocomposites. Propell Explos Pyrot. 2013;38:386-93.

15. Y. Wang, R.N. Dave, Pfeffer R. Polymer coating encapsulation of nanoparticles using a supercritical anti-solvent process. Journal of Supercritical Fluids. 2004;28:85-99.

16. Rodrigues M, Peirico N, Matos H, Azevedo E Gomes de, Lobato M R, Almeida A. J. Microcomposites theophylline/hydrogenated palm oil from a PGSS process for controlled drug delivery system. J Supercrit Fluids. 2004;29:175-84.

17. Tsutsumi A, Nakamoto S, Mineo T, Yoshida K. A novel fluidized-bed coating of fine particles by rapid expansion of supercritical fluid solutions. Powder Technol. 1995;85:275-8.

18. Mishima K, Matsuyama K, Tanabe D, Yamauchi S, Young T J, Johnston K. P. Microencapsulation of proteins by rapid expansion of supercritical solution with a nonsolvent. AIChE J. 2000;46:857-65.

19. Glebov E M, Yuan L, Krishtopa L G, Usov O M, Krasnoperov L. N. Coating of metal powders with polymers in supercritical carbon dioxide. Ind Eng Chem Res. 2001;40:4058-68.

20. Kim J H, Pastón T E, Tomasko D. L. Microencapsulation of naproxen using rapid expansion of supercritical solutions. Biotechnol Prog. 1996;12:650-61.

21. Moon R S, Khamkar G S, Pede P V, Mali D K, Kadam M. V. A review: methods for enhancing bioavailability of drug. Int J Pharm Tech. 2011;3:912-26.

22. Li Z, Jiang H, Xu C, Gu L. A review: using nanoparticles to enhance absorption and bioavailability of phenolic phytochemicals. Food Hydrocoll. 2015;43:153-64.

23. Kesavan K, Balasubramaniam J, Kant S, Singh P N, Pandit J. K. New approaches for optimal bioavailability of ocularly delivered drugs: Review. Curr Drug Deliv. 2011;2:172-93.

24. Hetal T, Bindesh P, Sneha T. A review on techniques for oral bioavailability enhancement of drugs. Int J Pharm Sci Rev Res. 2010;4:203-23.

25. Manikandan P, Subramanian N. Improving solubility and bioavailability of poorly water soluble drugs by solid dispersion technique - a review. Int J Pharm Sci Rev Res. 2013;23:220-7.

26. Sharma P, Garg S. Pure drug and polymer based nanotechnologies for the improved solubility, stability, bioavailability and targeting of anti-HIV drugs. Adv Drug Deliver Rev. 2010;63:491-502.

27. Patil J S, Kadam D V, Marapur S C, Kamalapur M. V. Inclusion complex system; a novel technique to improve the solubility and bioavailability of poorly soluble drugs: a review. Int J Pharm Sci Rev Res. 2010;2:29-34.

28. Subramaniam B, Rajewski R A, Snavely K. Parmaceutical processing with supercritical carbon dioxide. J Pharm Sci. 1997;86:885-90.

29. Cardea S, Baldino L, Scognamiglio M, Reverchon E. 3D PLLA/Ibuprofen composite scaffolds obtained by a supercritical fluid assisted process. J Mater Sci: Mater Med. 2014;25:989-98.

30. Babazadeh M. Synthesis and study of controlled released of ibuprofen from the new acrylic type polymers. Int J Pharm. 2006;316:68-73.

31. Hasnain M S, Nayak A. K. Solubility and dissolution enhancement of ibuprofen by solid dispersion technique using PEG 6000-PVP K 30 combination carrier. Chem: Bulgarian J Sci Edu. 2012;21:118-32.

32. Rupapara V, Patel J, Chavda V, Soniwala M. Organic volatile impurities and their regulatory limits: a pharmaceutical perspective. Mintage J Phar Med Sci.

2013;2:10-4.

33. Antonov E N, Minaeva S A, Popov V. K. A study of ibuprofen solubility in supercritical carbon dioxide by fourier-transform infrared spectroscopy. Russ J Phys Chem B. 2013;7:849-53.

34. Hezave A Z, Esmaeilzadeh F. Micronization of drug particles via RESS process. J Supercrit Fluids. 2010;52(84-98).

35. Cocerol M J, Mart ń A, Mattea F, Varona S. Encapsulation and co-precipitationi processes with supercriticcal fluids: fundamentals and applications. J Supercrit Fluids. 2009;47:546-55.

36. Kim J -T, Kim H -L, Ju C.-S. Micronization and characterization of drug substances by RESS with supercritical CO_2. Korean J Chem Eng. 2010;27:1139-44.

37. Bolten D, Turk M. Micronisation of carbamazepine through rapid expansion of supercritical solution (RESS). J Supercrit Fluids. 2012;62:32-40.

38. Stepanov V, Anglade V, Hummers W A B, Bezmelnitsyn A V, Krasnoperov L. N. Production and sensitivity evaluation of nanocrystalline RDX-based explosive compositions. Propell Explos Pyrot. 2011;36:240-6.

39. Cerclier O, Estienne J. An X-ray powder diffraction study on explosives. Mater Sci Forum. 1994;169:749-54.

40. Scherrer P. Nachr Ges Wiss Gottingen. 1918;2:98-100.

41. Gubicza J. X-ray line profile analysis in materials science: IGI Global; 1969.

42. Stokes A R, Wilson A. J. C. The diffraction of X rays by distorted crystal aggregate - I. Proceedings of the Physical Society. 1944;56:174-81.

43. Williamson G K, Hall W. H. X-ray line broadening from field aluminium and wolfram. Acta Metallurgica. 1953;1:22-31.

44. Matsunaga T. Formation of RDX nanoparticles by rapid expansion of supercritical solutions: in situ characterization by laser scattering: New Jersey Institute of Technology; 2007.

45. Feau C, Klein E, Dosche C, Kerth P, Lebeau L. Synthesis and characterization of coumarin-based europium complexes and luminescence measurements in aqueous media. Org Biomol Chem. 2009;7:5259-70.

46. Young T J, Johnston K P, Mishima K, Tanaka H. Encapsulation of lysozyme in a biodegradable polymer by precipitation with a vapor-over-liquid antisolvent. J Pharm Sci. 1999;88:640-50.

47. Haubruge H G, Jonas A M, Legras R. Staining of poly (ethylene terephthalate) by ruthenium tetroxide Polymer. 2003;44:3229-34. Epub Mar 18, 2003.

48. Makinson J D, Lee J S, Magner S H, Angelis R J De, Weins W N, Hieronymus A. S. X-ray diffraction signatures of defects in nanocrystalline materials. Adv X-ray Anal. 1998;42:407-11.

49. Sperling L. H. Introduction to physical polymer science. New Yok: John Wiley & Sons, Inc.; 2006. 71-4 p.

50. Loth H, Hemgesberg E. Properties and Dissolution of Drugs Micronized by Crystallization from Supercritical Gases. Int J Pharm. 1986;32:265-367.

51. Hirenkumar K, Makadia K, Siegel S. J. Poly lactic-co-glycolic acid (PLGA) as biodegradable controlled drug delivery carrier. Polymers. 2011;3:1377-97.

52. Haglund B. O. Solubility studies of polyethylene glycols in ethanol and water. Thermochimica Acta. 1987;114:97-102.

53. Garzon C, Martinez F. Temperature dependence of solubility for ibuprofen in some organic and aqueous solvents. J Solution Chem. 2004;33:1379-95.

54. Lalla J K, Chugh N. N. Biodegradable polymer: polylactic acid part II: evaluation as matrix material for controlled release and as a microencapsulating agent. Indian Drugs. 1990;27:516-22.

55. Jia Z, Tian C. Quantitative determination of polyethylene glycol with modified dragendorff reagent method. Desalination. 2009;247:423-9.

56. Rivera-Leyva J C, Garcia-Flore M, Valladares-Mendez A, Orozco-Castellanos L M, Martinez-Alfaro M. Comparative studies on the dissolution profiles of oral ibuprofen suspension and commercial tablets sing biopharmaceutical classification system criteria. Indian J Pharm Sci. 2012;74:312-8.

57. Masters K. Spray drying handbook 4th Ed. New York, NY: Wiley; 1985. 171 p.

58. Matsunaga T, Chernyshev A V, Chesnokov E N, Krasnoperov L. N. In situ optical monitorning of RDX nanoparticles formation during rapid expansion of supercritical CO_2 solutions. Phys Chem Chem Phys. 2007;9:5249-59.

59. Miller-Chou B A, Koening J. L. A review of polymer dissolution. Prog Polym Sci. 2003;28:1223-70.

60. Crank J, Park G. S. Diffusion in polymers. New York, NY: Academic Press; 1968.

61. Brandrup J, Immergut E H, Grulke E. A. Polymer handbook 4th ed. New York, NY: Wiley; 1999.

62. Fedors R. F. A method for estimating both the solubility parameters and molar volumes of liquids. Polym Eng Sci. 1974;14:147-54.

63. Hussain Y, Wu Y T, Ampaw P J, Grant C. S. Dissolution of polymer films in supercritical carbon dioxide using a quartz crystal microbalance. J Supercrit Fluids. 2007;42:255-64.

64. O'Neil M L, Cao Q, Fang M, Johnston K P, Wilkinson S P, Smith C D, et al. Solubility of homopolymers and copolymers in carbon dioxide. Ind Eng Chem Res. 1998;37:3067-79.

65. Rindfleisch F, DiNoia T P, Mchugh M. A. Solubility of polymers and copolymers in supercritical CO_2. J Phys Chem. 1996;100:15581-7.

66. Sodergard A, Stolt M. Properties of lactic acid based polymers and their correlation with composition. Prog Polym Sci. 2002;27:1123-63.

67. Mertdogan C A, DiNoia T P, Mchugh M. A. Impact of backbone architecture on the solubility of fluorocopolymers in supercritical CO_2 and halogenated supercritical solvents: comparison of poly(vinylidene fluoride-co-22 mol% hexafluoropropylene) and poly(tetrafluoroethylene-co-19 mol% hexafluoropropylene). Macromolecules. 1997;30:7511-5.

68. Brandrup J, Immerqut E H, Grulke E. A. Polymer handbook. 4th ed. New York: Wiley-Interscience; 2003.